DEEP INELASTIC SCATTERING AT HERA

Gregorio Bernardi*
LPNHE Paris
4 Place Jussieu, Tour 33 R.d.C.
Universités Paris VI et VII
75232 Paris CEDEX 05, France

Representing the H1 and ZEUS Collaborations

ABSTRACT

The inclusive measurements performed between 1994 and 1997 in Deep Inelastic Scattering at HERA are reviewed. The subjects covered include the measurement of the proton structure function $F_2(x, Q^2)$ at low and high Q^2, the comparison of F_2 with Next to Leading Order DGLAP evolution, and the determination of the longitudinal structure function F_L at high y. The study of the charm density in the proton and the extraction of F_2^c are presented, as well as different extractions of the gluon density $xg(x, Q^2)$ in the proton. The measurements of the double differential cross-sections at high Q^2 are shown both in neutral and charged current with an emphasis on the high x region. Measurements of the W propagator mass are presented.

*e-mail: gregorio@mail.desy.de

1 Introduction

The first two years after the commissioning of the first *ep* collider HERA in May 1992 were devoted in deep inelastic scattering (DIS) to the observation of the new processes which would become the main subject of study nowadays in DESY. The observation of the rise of the F_2^p proton structure function at low x[1-4] was the first of this type of measurement which is still progressing in terms of precision. The structure function results provide the opportunity to test QCD in new kinematic regimes, to extract the gluon and the charm density in the proton, and in the future, to measure α_S. The measurement of these quantities can also be made at HERA in an exclusive way by measuring the charm induced processes, or the rates of events with two or three jets. The observation of high Q^2 charged and neutral current events,[5,6] with very low statistics at that time, but in an excellent experimental environment, allowed a glimpse of the future of the HERA collider. The subsequent years (1995,1996,1997) are covered in this report. The increased integrated luminosity and the improvements of the detector allowed for the precise measurements of the phenomena mentioned above, besides many others. Indeed in 1995, the H1 collaboration upgraded the backward detectors of the experiment, introducing in particular a more precise drift chamber (BDC) to measure the polar angle of the scattered electron, and a new SPACAL calorimeter with better hadronic containment, better granularity, and better angular acceptance. Similarly, ZEUS upgraded the backward part of its detector by introducing a beam pipe calorimeter (BPC) which allows for the measurement of the scattered positron at Q^2 as low as 0.1 GeV^2. The results obtained have fulfilled the expectations and a new step in precision could thus be reached for the low Q^2 physics.

In this report, after an introduction in section 2 to deep inelastic scattering and its basic measurement issues, the following points will be reviewed: in section 3 the results on cross-sections and structure functions at low Q^2 are presented in the context of the transition between the DIS and photoproduction regime. In section 4, the structure function F_2 results in the intermediate Q^2 region (a few GeV^2) are given followed in section 5 by its QCD analysis. Section 6 is devoted to the longitudinal structure function F_L determination, section 7 to the measurement of the charm component of the structure function, and section 8 to the measurements of the gluon density $xg(x, Q^2)$ in the proton. In section 9 are presented the cross-section measurements at high Q^2 and the extraction of M_W from these data.

2 Deep Inelastic Scattering at HERA

2.1 Basics of DIS

To define the kinematic variables used in DIS measurements, let us use the following graph which is an illustration of the basic DIS process. The exchanged boson is a photon in most of the cases, but the exchange of Z^0 or $W^\pm$ becomes sizable at high Q^2. The graph represents a neutral current event (NC). For a charged current event (CC) which occurs via $W^\pm$ exchange, the outgoing lepton becomes a neutrino, and the kinematics can thus be only reconstructed from the hadronic final state. The variables x, y, Q^2, and W^2 are defined in the following way:

4-momentum transfer:
$Q^2 = -q^2 = -(k - k')^2$

parton momentum fraction:
$x = Q^2/(2p \cdot q)$

fractional energy transfer:
$y = p \cdot q/(p \cdot k)$

mass^2 of hadronic system:
$W^2 = (p + q)^2 \approx Q^2/x.$

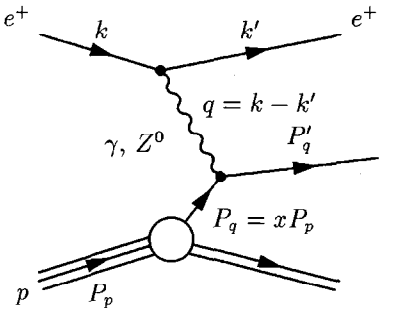

At low Q^2, *i.e.*, in the region in which the interaction proceeds essentially via photon exchange, the structure function F_2 of the proton can be derived from the double differential cross-section. In the naive Quark Parton Model (QPM) we have

$$\frac{d^2\sigma^{e^\pm p}}{dxdQ^2} = \frac{2\pi\alpha^2}{Q^4 x}\left[1 + (1-y)^2\right] F_2(x, Q^2) = \frac{2\pi\alpha^2}{Q^4 x} Y_+ F_2(x, Q^2) \qquad (1)$$

and F_2 is related to the quark densities:

$$F_2(x) = x\sum_{i=1}^{n_f} e_i^2 (q_i(x) + \overline{q}_i(x)). \qquad (2)$$

The longitudinal structure function F_L is equal to 0 in the QPM, following the Callan-Gross relation. In Quantum Chromodynamics (QCD) the presence of spin 1 partons (the gluons) changes the picture: F_2 becomes a function of x and Q^2, and a non-zero

F_L must be taken into account:

$$\left.\frac{d^2\sigma^{e^\pm p}}{dx\,dQ^2}\right|_{Born} = \frac{2\pi\alpha^2}{xQ^4}\left[Y_+F_2(x,Q^2) - y^2F_L(x,Q^2)\right]. \quad (3)$$

Not shown in the previous equations is the influence of the QED radiative corrections which are precisely known, with a precision of the order of 1%, and for which the cross-section is corrected. The case of DIS at higher Q^2 which involves W and Z exchange and electroweak radiative corrections will be treated in section 9.

2.2 Kinematics and Measurement

Measured quantities in **inclusive** processes:

e^+: energy E'_e
polar angle θ_e

hadrons: $\Sigma = \sum_i (E_i - p_{z,i})$
$p_{T,h} = \sum_i p_{T,i}$
$\gamma_h = 2 \cdot \arctan \Sigma / p_{T,h}$

(The sums runs over all particles of the hadronic final state).

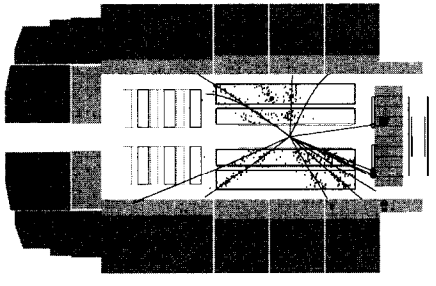

The selection of NC DIS events at HERA requires the detection of an electromagnetic cluster representing the scattered electron* above a certain energy threshold which is typically around 5 GeV, and the presence of a reconstructed interaction vertex in order to reject the beam associated background and to improve the reconstruction quality. Further requirements are applied depending on the analyses but we refer to the original papers for more details on this matter.[3,4] The selection of CC DIS events requires the detection of missing transverse energy which represents the energy carried away by the scattered neutrino. This selection is more difficult than in the NC case, since the energy of the hadronic final state is shared among many softer particles, hence the difficulty to have a low energy trigger, and to reject unambiguously the background which can come either from external sources (cosmic muons, parasitic muons produced by the off-beam protons) or from ep interactions, such as photoproduction events with jet production.

*HERA can run both with e^+ and e^-, but here "electron" is used both for e^+ and e^-.

The kinematics can be reconstructed at HERA with different methods for the neutral current (NC) events [electron only (e), Sigma (Σ), Double Angle (DA) or some combinations of these methods], but only one (hadrons only, h) for the charged current (CC). In general H1 uses for the NC the e, the Σ and the $e\Sigma$ methods, since they complement each other, while ZEUS uses the e method at low Q^2 and the DA or the PT methods at higher Q^2 since these last two methods are less sensitive to the reconstruction of the positron energy. The methods used for kinematic reconstruction are reviewed[7] and defined in the following way:

- Electron Method: $y_e = 1 - E'_e/E_e \sin^2\theta_e/2 \quad Q^2_e = 4E'_eE_e\cos^2\theta_e/2.$
  It is most precise at low x but quite sensitive to QED radiation, with corrections to the cross-section of the order of 30% in the absence of specific kinematic cuts. It has also an excellent Q^2 resolution in the full kinematic range, but a poor resolution in x at low y which necessitates the use of an alternative method in this region.
- Hadron Method[8]: $y_h = \Sigma/2E_e \qquad Q^2_h = p^2_{T,h}/(1-y_h).$
  This method does not allow for a precise determination of the kinematics but it is the only inclusive method for charged current events.
- Σ Method[9]: $y_\Sigma = \Sigma/(\Sigma + E'_e(1-\cos\theta_e)) \quad Q^2_\Sigma = E^2_e\sin^2\theta_e/(1-y_\Sigma).$
  The Σ method can be used in the full kinematic range since it has good x and Q^2 resolution both at high and low y. Furthermore, it is essentially independent of QED initial state radiation, thereby allowing an experimental cross-check of the radiative corrections by a comparison with the cross-section measurement done with the electron method.
- Double Angle method:[10] x_{DA}, Q^2_{DA} are determined from θ_e, γ_h.
  This method, which uses only the angle of the electron and the inclusive hadronic angle, leads to a high precision at high Q^2, but it is sensitive to QED radiation, and becomes imprecise at low γ_h, *i.e.*, at low y. Its strong point is to be independent of the electron energy and, in first order, of the hadronic energy scale. It is thus also used for calibration purposes.
- $e\Sigma$ Method[9]: $x_{e\Sigma} = x_\Sigma \qquad Q^2_{e\Sigma} = Q^2_e.$
  The simple combination of the advantages of the electron and Σ methods is very precise over the whole kinematic range, allowing in particular for an extension of the measurement to high x.
- PT Method[4]: x_{PT}, Q^2_{PT} are obtained from the DA method in which γ_h is

replaced by $\gamma_{PT} \equiv 2 \cdot \arctan \frac{2E_e \cdot \Sigma}{[\Sigma + E_e(1-\cos\theta_e)]p_{T,e}}$, not using therefore the unprecise measurement of $p_{T,h}$ from the hadronic final state.

Once the kinematics of the events are determined, the measurements rely on the following main points: The NC data are binned in (x, Q^2) with about 5 bins/order of magnitude in x and 10 bins/order of magnitude in Q^2. The CC data due to their lower resolution are binned with about 3 bins/order of magnitude in x and Q^2. The purity and stability[†] of an (x, Q^2) bin are requested to be typically greater than 30%, for the measurement to be done in that bin. From the selected events the *ep* background (mainly due to misinterpreted photoproduction events) is then subtracted. The acceptance corrections are performed using the simulation which describes well the data. The systematic errors associated with the measurement are split into a correlated and an uncorrelated contribution for each x, Q^2 bin. The total errors vary for NC cross-sections between 5% and 25% from low to high Q^2, for which the statistical error dominates. For the CC cross-sections, which are based on much lower statistics, the error range is between about 15% to 30%. The luminosity is known within 1.5–2.5% at HERA, depending on the year and the various beam conditions. The radiative corrections are known either from Monte Carlo or from analytical programs. Thus, after applying bin center corrections, the Born cross-section $\frac{d^2\sigma}{dxdQ^2}\Big|_{Born}$ can be measured at a given x and Q^2.

2.3 Overview of the F_2 Measurements at HERA

With the first HERA data taking in 1992, H1 and ZEUS have observed the strong rise of $F_2(x, Q^2)$ at low x at fixed Q^2. This rise has been confirmed with higher precision in 1993 and 1994,[3,4] and a good agreement between HERA and the older fixed target experiments has been observed. Next to Leading Order (NLO) QCD has been shown to give a good description of the data at Q^2 as low as 1.5 GeV^2 and has allowed for the extraction of the gluon density, which was also observed to rise towards low x.

H1 and ZEUS have brought with these measurements, and with the more recent measurements which will be described in more detail below, a major extension of the kinematic range of the F_2 measurement, as can be observed in Fig. 1, permitting a significant contribution to the understanding of the proton structure and of the theory of strong interactions.

[†]The stability (purity) is defined as the fraction of events which originate from a bin and which are reconstructed in it, divided by the number of generated (reconstructed) events in that bin.

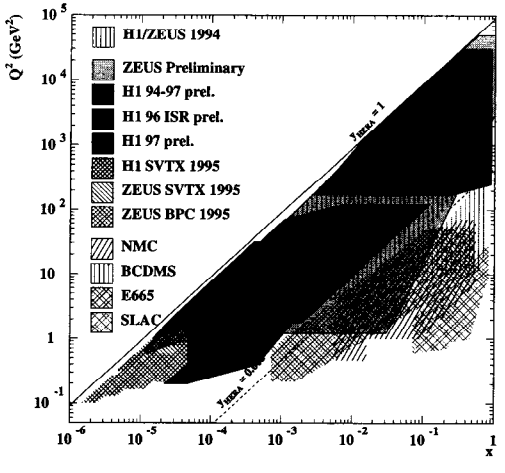

Figure 1: *Kinematic plane indicating the x and Q^2 regions of proton structure function measurements from HERA and fixed target experiments.*

- The extension to low x, below 10^{-5}, has permitted us to test successfully the low x limit of perturbative QCD.
- The extension to high x, up to 0.65 at $Q^2 > 500$ GeV^2, made possible the probing of the valence quark region at high Q^2.
- Reaching y as low as 0.005 provided F_2 measurements in overlap with fixed target experiment ones, which were thus shown to be consistent without extrapolation.
- The high y region measured at medium Q^2 ($\simeq$ 3–100 GeV^2), up to 0.82, displayed the sensitivity of the cross-section to F_L.
- By measuring very low Q^2 events, down to $Q^2 = 0.1$ GeV^2, the transition region from photoproduction to DIS has been explored.
- The increasing integrated luminosity permits us to approach the HERA kinematic limit, and at the highest Q^2 presently reached (30000 GeV^2) in NC events, the sensitivity to electroweak effects ($\gamma - Z^0$ interference) has been demonstrated.

We will now review the recent results obtained in '95, '96, and '97 in three main regions of Q^2, the low Q^2 region which extends from 0.1 to a few GeV^2, the intermediate Q^2 region, from a few GeV^2 to about 100 GeV^2, and the high Q^2 region, up to 30000

GeV^2. This subdivision corresponds to three main physics regimes of deep inelastic scattering.

3 The Low Q^2 Region

Experimentally, since Q^2 is well determined by the scattered electron measurement with $Q^2 = 4E'_e E_e \cos(\frac{\theta_e}{2})$, we can see that this kinematic regime can be optimally explored by[11,12]:

- Shifting the interaction vertex towards the forward direction (defined as the proton direction), by slightly changing the parameters of the collider, hence increasing the angular acceptance for the electron.
- Adding dedicated low angle detectors (BPC in ZEUS) or upgrading the backward calorimeter to improve, among others, its hermeticity (SPACAL in H1).
- Selecting "radiative" events, *i.e.*, events in which the incident lepton has emitted a photon before the deep inelastic collision, which have thus a lower center of mass energy, hence a lower Q^2, for a given measured angle and energy. The results using this technique are not reviewed in this paper.

These three techniques have been used by the two HERA experiments to measure F_2 at low Q^2 ($Q^2 \lesssim 5$ GeV^2).

3.1 $F_2(x, Q^2)$ at Low Q^2

In Fig. 2 are shown the measurements taken in shifted vertex position by H1[11] and ZEUS[12] in 1995. The main observations are that F_2 rises at low x, even at the lowest Q^2 = 0.11 GeV^2 measured at HERA. The lowest x point is reached at 6×10^{-6}. The rise becomes less pronounced when Q^2 decreases, and no discontinuous behavior can be observed from the data.

From a theoretical point of view, two approaches are attempting to describe this low Q^2 regime.

- The Regge approach as in the Donnachie-Landshoff model.[15] Here the total cross-section $\sigma^{tot} \propto W^{2\alpha_P}$, α_P is Q^2 independent and determined from hadron data ("soft Pomeron hypothesis"). This approach describes successfully the photoproduction data.

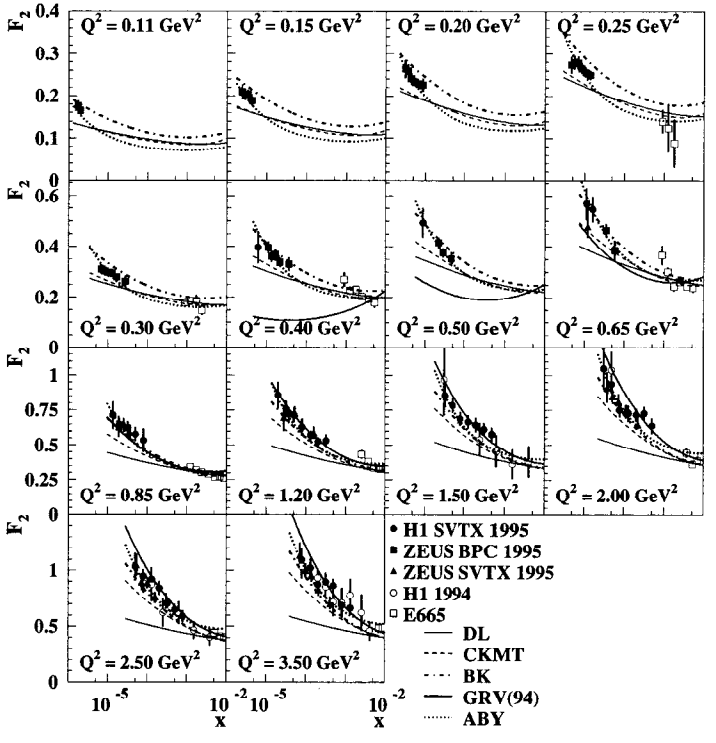

Figure 2: *F_2 measurements at very low Q^2 compared to various parametrizations. SVTX refers to data taken in shifted vertex position. BPC refers to data taken in shifted vertex position with the BPC detector (see text).*

- The perturbative QCD (pQCD) approach which is well known to describe successfully the DIS regime at high Q^2. It has been conjectured in the GRV[16] model that using valence-like partons at a very low starting scale ($Q_0^2 \sim 0.4$ GeV^2) and evolving them according to the DGLAP[17] evolution equation may describe successfully the DIS data at low Q^2.

The following conclusions can be drawn from the comparisons in Fig. 2 of the results with the GRV and DL models (the comparison to the other models will be commented on in the next section).

- pQCD (*i.e.*, GRV) describes the data down to $Q^2 \lesssim 1$ GeV^2. The breakdown of perturbative QCD happens at lower Q^2 than expected, but is visible at $Q^2 \simeq 0.5$–0.8 GeV^2.
- The DL Regge Model prediction is too low at low x, even at very low Q^2, but it describes the data at $Q^2 \lesssim 2$ GeV^2 and $x \gtrsim 10^{-3}$.

Thus there is no obvious way to reconcile these two approaches, and the transition region is not clearly visible in these measurements.

A better picture can be achieved by interpreting these F_2 measurements as a cross-section measurement of the virtual photon – proton ($\gamma^* p$) interaction. Indeed in the Hand convention for the flux of virtual photons,[13] the total $\gamma^* p$ cross-section can be related to the F_2 structure since at low x the lifetime of the virtual photon in the proton rest frame is large compared to the $\gamma^* p$ interaction time.[14] The ep scattering is thus interpreted as a $\gamma^* p$ scattering with total cross-section:

$$\begin{aligned} \sigma_{tot}^{\gamma^* p}(W^2, Q^2) &= \sigma_L^{\gamma^* p} + \sigma_T^{\gamma^* p} \simeq \frac{4\pi\alpha^2}{Q^2} F_2 \equiv \sigma_{eff}^{\gamma^* p}(W^2, Q^2) \\ W^2 &\approx Q^2/x \quad \text{at low } x. \end{aligned}$$

These measurements on $\sigma_{eff}^{\gamma^* p}$ at low Q^2 ($\approx 0.1 - 5$ GeV^2) can be compared to the photoproduction total cross-section $\sigma_{tot}^{\gamma p}$ determined at HERA at $Q^2 \approx 0$ in order to understand the transition between the photoproduction and the DIS regimes.

The transition between these two descriptions of the data is visible in Fig. 3a. The $\gamma^* p$ cross-section decreases steeply in the DIS regime, while it is expected to stay constant in the photoproduction regime. The smooth turning point happens at Q^2 between 0.1 and 1 GeV^2 as can be seen by the measurements at W between 115 and 245 GeV (corresponding, at $Q^2 = 1$ GeV^2, to x between $1.7 \cdot 10^{-5}$ and $0.8 \cdot 10^{-4}$). Further results at $Q^2 < 0.1$ GeV^2 will become available with the analysis of more recent data and will complement these measurements and provide a complete coverage of the transition region.

A further requirement on the models is to be able to describe the W^2 behavior of the total cross-section, as shown in Fig. 3b.

3.2 Models for the Transition DIS $\rightarrow \gamma$p

The new data obtained at HERA revived the theoretical attempt to describe the DIS $\rightarrow \gamma$p transition and additional models were developed. Two different non-perturbative

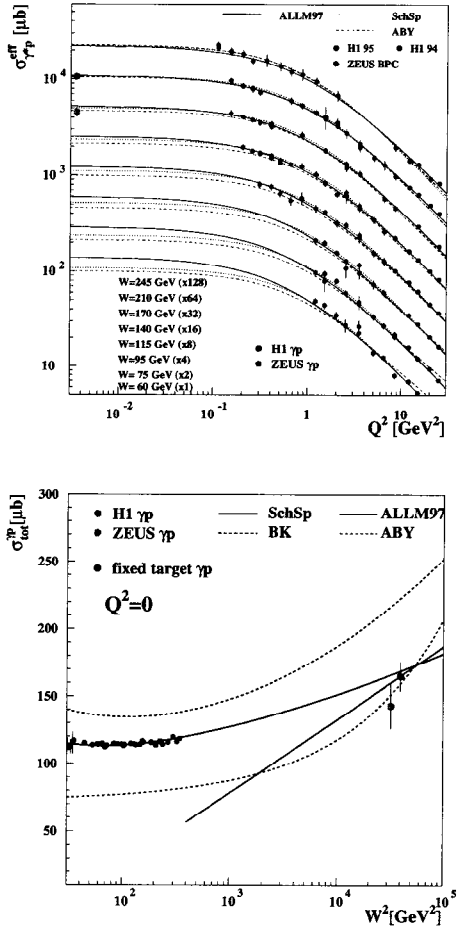

Figure 3: *$\gamma^* p$ cross-section as a function of Q^2 for different values of W. The transition between the photoproduction and the DIS behavior is visible between 0.1 and 1 GeV^2 (left). Total γp cross-section as a function of W^2 (right). The data (points) are compared with different parameterizations (see text).*

approaches have been considered to understand this transition, namely Regge theory (as briefly sketched above) and the vector meson dominance model (VMD). VMD relates the hadronic interactions of the photon to a sum over interactions of the ρ^0, ω and ϕ vector meson states.[18,19] To accommodate deep inelastic scattering data, the sum has to be extended to an infinite number of vector mesons giving the generalized vector dominance model (GVMD).[20]

Since neither the non-perturbative VMD and DL approaches nor pQCD are describing the Q^2 behavior of F_2 over the complete range from photoproduction to very large Q^2 deep inelastic scattering (DIS), the following models mix these approaches.

- The Badelek and Kwiecinski (BK) model uses a VMD approach at low Q^2 and pQCD at Q^2 above 1 GeV^2. It gives a good description in the transition region (Fig. 3a), but predicts a too large photoproduction cross-section (Fig. 3b).
- Schildknecht and Spiesberger (SchSp)[21] have revived the GVMD approach. The domain of application of their model is expected to be $0<x<0.05$, $0<Q^2<350$ GeV^2 and $W>30$ GeV. However, the photoproduction behavior is not described in this model, as shown in Fig. 3b.
- Adel, Barreiro, and Yndurain (ABY)[23] assume that pQCD is applicable to the lowest values of Q^2. To modify the behavior of F_2 which becomes flat as a function of x for Q^2 values below 1 GeV^2, a hard contribution ($\propto x^{-\lambda_s}, \lambda_s = 0.48$) is introduced, preventing the flattening at low x even at low Q^2 values. This model gives a fair description of the transition region, but fails in the photoproduction region.
- Abramowicz *et al.* (ALLM97)[22] assume that the total $\gamma^* p$ cross-section consists of two contributions which distinguish Reggeon and Pomeron exchange, and the power λ is assumed to vary with Q^2, in a similar way as pQCD in the high Q^2 region. This model currently describes all available data, but, contrarily to the others, makes use also of the photoproduction data to constrain its parameters.
- A Regge fit (including Pomeron and Reggeon contributions)[24] gives a good description of the very low Q^2 ZEUS data (which have been extrapolated to $Q^2 = 0$ using a GVDM fit) and of the low W γp data (see Fig. 4a). The resulting α_P is 1.010 ± 0.002. The photoproduction total cross-sections measured at HERA are not well described by this fit (Fig. 4b).

In conclusion, the Regge or pQCD approach cannot describe the data on its full range, but models such as ABY,[23] SchSp,[21] or ALLM97,[22] which are decribed in the next section and which all include the HERA data when fitting their parameters can give a good description of the data but for the total photoproduction cross-section. However, the ALLM97 parametrization, which makes use also of the low W photoproduction data, can give a good description of the complete W dependence of the γp cross-sections, as can be seen in Fig. 3.

3.3 Evolution of the Slope of $F_2(x, Q^2)$ vs x

The effective x slope at fixed Q^2 has been fitted at low x assuming $F_2 \propto x^{-\lambda}$ (for $x < 0.1$ in H1 or $x < 0.01$ in ZEUS). We thus have

$$\lambda \approx \frac{d \ln F_2}{d \ln 1/x}. \tag{4}$$

The precision obtained on λ with the recent data (H1 1997) is typically $\simeq 1\%$(stat) $\oplus 5\%$(syst). The rise of F_2 is thus quantified, and this effective slope decreases from values of 0.3 at $Q^2 \simeq 30$ GeV^2 down to 0.1 at $Q^2 \simeq 1$ GeV^2 displaying a smooth transition between the pQCD regime where λ is rapidly evolving as a function of Q^2 and the γp regime where λ is essentially constant.

4 Measurements of $F_2(x, Q^2)$ in the DIS Regime

New high precision measurements of $F_2(x, Q^2)$ with the NC data collected in 1996-97 by H1 and ZEUS have been released in a preliminary form in 1998.[25,26] Depending on the kinematic region and on the experiment, the integrated luminosity of the data varies between 7 and 27 pb^{-1}. The analyses follow closely the strategy adopted for the 1994 published papers; however, the higher statistics have made possible a substantial reduction of the total errors on the measurements. Below 100 GeV^2, they are typically below $\approx 1\%$ for the statistical error and about 4% for the systematic error, except at high y for which the systematic error grows up to about 12%. The main sources and the magnitude of systematic errors are:

- the electron energy scale: $\frac{\delta E_e}{E_e} = 0.5$–$1\%$,
- the hadronic energy scale: $\frac{\delta E_h}{E_h} = 2$–$3\%$,
- the electron identification: 1–2%,
- the photoproduction background: 1–2% at high y,

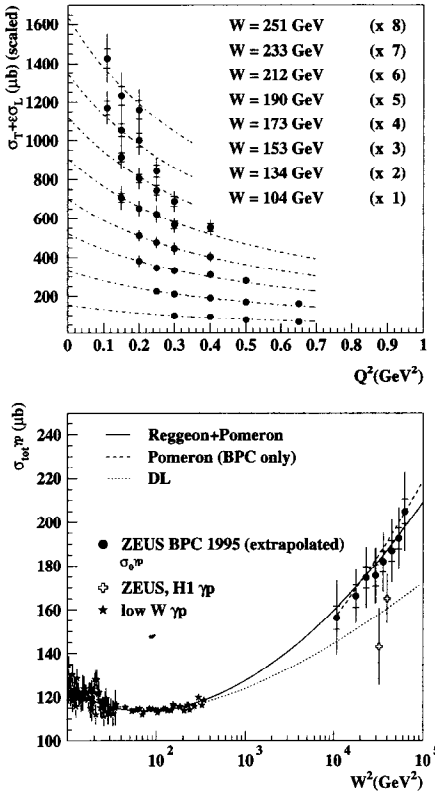

Figure 4: *Upper plot.* ZEUS BPC measurements of the total cross-section $\sigma_T + \epsilon\sigma_L$ in bins of W as a function of Q^2 and the GVMD fit to the data. *Lower plot.* $\sigma_{tot}^{\gamma p}$ as a function of W^2. The ZEUS BPC95 points are extrapolated to $Q^2 = 0$ using the GVMD fit. Also shown are the direct measurements of the total photoproduction cross-section from H1, ZEUS, and earlier experiments at low energies. The curves show Regge fits: the original DL fit[15] to the low W data (dotted); the Pomeron only fit to the BPC $\sigma_0^{\gamma p}$ data (dashed) and the Pomeron+Reggeon fit to the low W and BPC $\sigma_0^{\gamma p}$ data (full). See the ZEUS Collaboration[24] for more details.

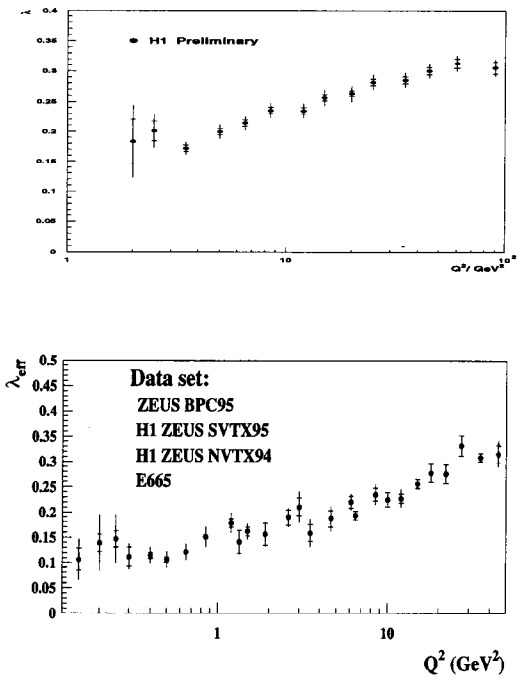

Figure 5: *Effective slopes of $F_2 \propto x^{-\lambda}$ for $x < 0.1$ (H1) and $x < 0.01$ (ZEUS).*

- the radiative corrections: 1–2%,
- the tracking efficiencies and vertex reconstruction 1–2%.

The ZEUS preliminary results are shown in Fig. 6 at fixed x as a function of Q^2. The coverage in x has been extended to higher x, yielding an increased overlap with the fixed target experiments, in which the agreement is good. The measurements are now performed over four orders of magnitude in Q^2 and x with relative precision better than 10% in most of the bins. Similar results have been obtained by H1, and are discussed below in conjunction with their QCD interpretation. In Fig. 7 are shown the ZEUS preliminary results at fixed Q^2 as a function of x for Q^2 between 1.5 and 27 GeV^2 (see also section 9 for results at higher Q^2). The rise in F_2 for $x \to 0$ is measured with improved precision.

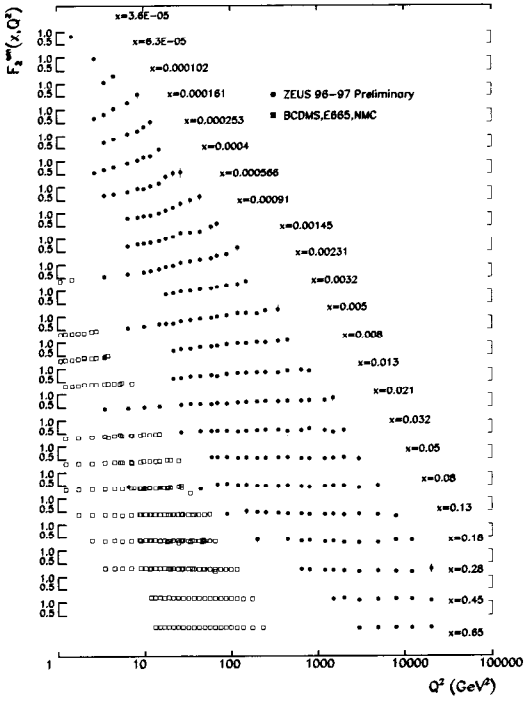

Figure 6: *Preliminary ZEUS measurements of F_2 as a function of Q^2 for fixed x from the 1996–1997 data (solid dots). The open rectangles show the results from the fixed target experiments.*

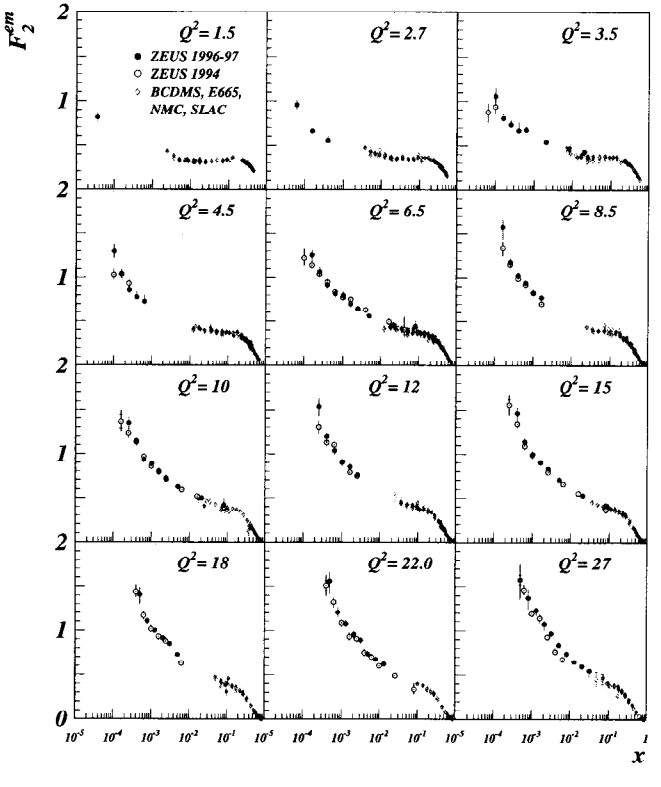

Figure 7: *Preliminary ZEUS measurements of F_2 as a function of x for fixed Q^2 values below 30 GeV^2 from the 1996-1997 data (solid dots). The diamonds show the results from the fixed target experiments. The inner error bars show the statistical errors, the outer error bars the quadratic sum of statistical and systematic errors.*

The extended precision obtained at HERA with the larger integrated luminosity allows for precise tests of perturbative QCD once they are used in combination with the fixed target experiment results. For a better understanding of the subsequent data interpretation, we will introduce the basics of QCD evolution equations and the QCD analyses performed by the two collaborations.

4.1 DGLAP Equations in QCD

Meaningful perturbative QCD tests necessitate going from the leading order expression for F_2 to its NLO version which relates it to the gluon density in the proton $xg(x)$:

$$\begin{array}{lll} \text{Leading Order:} & F_2(x) & = x\sum_{i=1}^{nf} e_i^2(q_i+\bar{q}_i) \\ \text{NLO } (\overline{\text{MS}}): & F_2(x,Q^2) & = x\sum_{i=1}^{n_f} e_i^2 C_q \otimes (q_i+\overline{q_i}) + C_g \otimes g \end{array}$$

in which the coefficient functions $C_{q,g}$ have been calculated to NLO. The singlet and non-singlet parton densities are defined as

$$\begin{array}{lll} x\Sigma & = \sum_{i=1}^{n_f}(xq_i + x\overline{q_i}) & \text{Singlet} \\ xq_{NS} & = \sum_{i=1}^{n_f}(xq_i - x\overline{q_i}) = xu_{val} + xd_{val} & \text{Non Singlet} \end{array}$$

and the DGLAP evolution equations of parton densities are given by:

$$\begin{array}{lll} \frac{\partial}{\partial t} q_{NS}(x,t) & = & \frac{\alpha_s(t)}{2\pi} P_{qq}^{NS} \otimes q_{NS}(y,t); \quad t = \log\frac{Q^2}{\Lambda^2} \\ \frac{\partial}{\partial t}\left(\Sigma(x,t), g(x,t)\right) & = & \frac{\alpha_s(t)}{2\pi}\left(P_{qq}, P_{qg}, P_{qg}, P_{gg}\right) \otimes \left(\Sigma(y,t), g(y,t)\right). \end{array}$$

The splitting functions P_{ij} are also known to NLO. A major property of these equations is the prediction of the Q^2 slope of $F_2(x,Q^2)$ for given parton densities at $Q^2 = Q_0^2$. However, no prediction on the x dependence at Q_0^2 is available from the theory, and this dependence must be obtained from a QCD fit to the data.

4.2 The H1 and ZEUS NLO-QCD Fit Programs

These programs use several assumptions which are often common to other widespread QCD analysis programs, like those from the MRS[59] or the CTEQ[48] groups.

- u, d, s are considered massless partons.
- the c density is obtained from Boson Gluon Fusion (BGF) calculated at NLO (Riemersma *et al.*) in the $\overline{MS}$ scheme, with the charm mass $m_c = 1.5$ GeV and the scale $\mu^2 = Q^2 + m_c^2$.

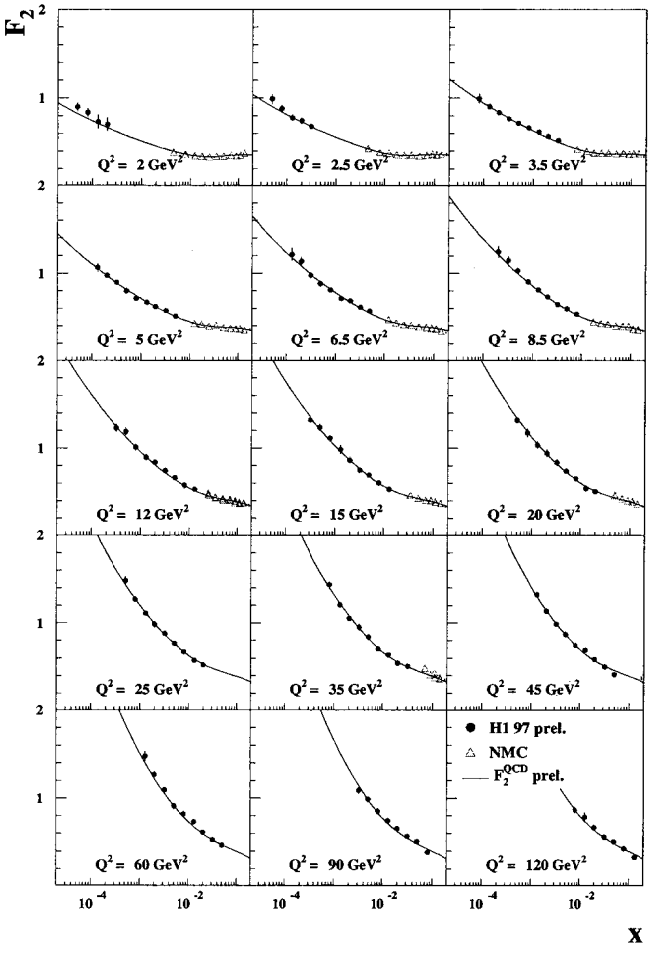

Figure 8: *H1 preliminary measurements on the 1997 data compared to the H1 NLO DGLAP fit which describes the data in the complete kinematic range.*

- A complete treatment of the correlated systematic errors is done, a particularity of the H1 and ZEUS QCD analysis.
- The theoretical uncertainties from α_s and m_c are taken into account.
- The Momentum Sum rule is assumed to be true: $\int_0^1 dx\, x(g+\Sigma) = 1$.
- The Quark Counting Rules are applied: $\int_0^1 dx\, u_v = 2$, $\int_0^1 dx\, d_v = 1$.
- The sea parton densities $\bar{u}$ and $\bar{d}$ are assumed equal. The strange parton density is assumed to be equal to 20% of the total sea parton density at Q_0^2.
- The data with x > 0.5 at low Q^2 are not used.

The input parton densities are parameterized as:

- $xg(x,Q_0^2) = A_g x^{B_g}(1-x)^{C_g}(1+D_g x+E_g\sqrt{x})$,
- $xu_v(x,Q_0^2) = A_u x^{B_u}(1-x)^{C_u}(1+D_u x+E_u\sqrt{x})$,
- $xd_v(x,Q_0^2) = A_d x^{B_d}(1-x)^{C_d}(1+D_d x+E_d\sqrt{x})$,
- $xS\,(x,Q_0^2) = A_s x^{B_s}(1-x)^{C_s}(1+D_s x+E_s\sqrt{x})$.

The datasets used in the QCD analysis are

- for ZEUS: ZEUS data (94+95) at $Q^2 > 1$ GeV^2, NMC[45] and BCDMS[60] p, d data,
- for H1: H1 data (94+95+96+97) at $Q^2 > 2$ GeV^2, NMC[45] and BCDMS[60] p, d data.

The H1 (ZEUS) experiment uses a Q_0^2 starting scale 2 (7) GeV^2. In both cases $\alpha_s(M_Z^2)$ is set to 0.118. For the H1 fit the gluon parametrization uses only three parametes, *i.e.*, $D_g = 0$ and $E_g = 0$ is assumed.

5 $F_2(x,Q^2)$ Compared to NLO QCD

To extract F_2 from the NC double differential cross-section, an assumption on F_L is made, based on QCD, which has however only a small influence on the results. In Fig. 8, the H1 preliminary measurements on the 1997 data are shown together with the NLO DGLAP fit which is describing them. The description is good in the whole phase space, but for the two lowest x points at 2 and 2.5 GeV^2 in Q^2 which display a tendency to lie above the QCD fit. Final results from H1 and ZEUS and final QCD analyses are needed however to draw strong conclusions from this observation. Also visible in the figure is the now well-known behavior of the rise of F_2 at low x, which becomes more

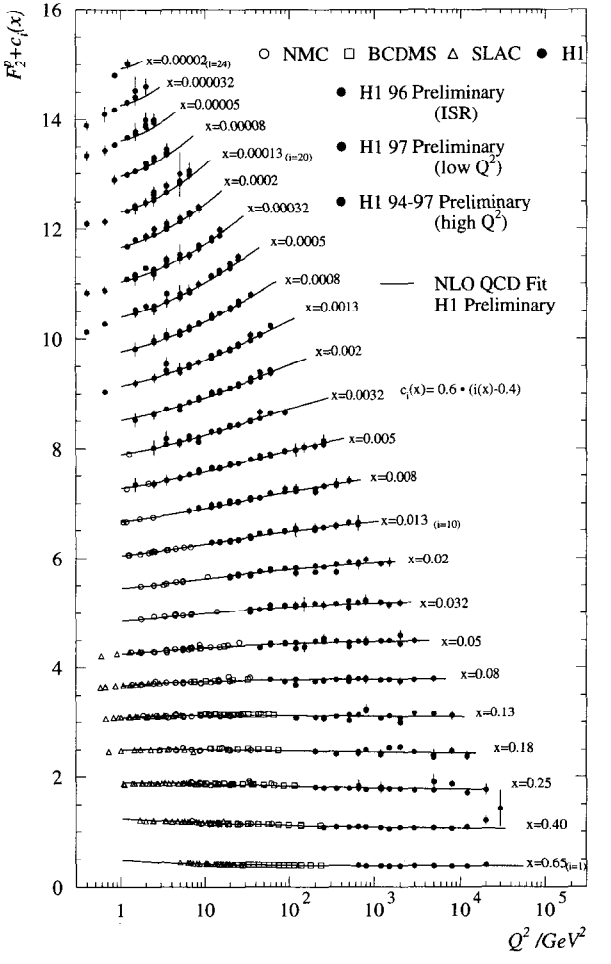

Figure 9: *Measurement of F_2 as a function of Q^2 in bins of fixed x. The H1 preliminary data are compared to the fixed target data, and to the H1 NLO QCD fit.*

steep when Q^2 increases. From this consequence of the DGLAP equations, Glück *et al.*[16] predicted the rise at low x of F_2 before any data at HERA was collected and without having to invoke BFKL effects.[27]

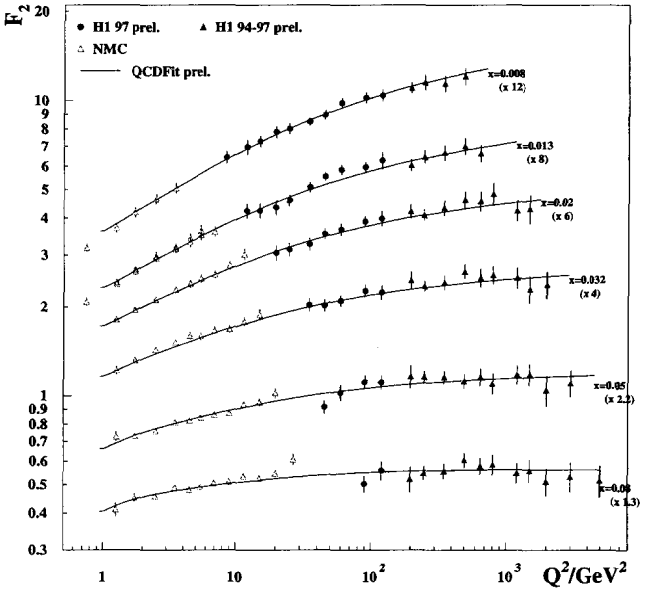

Figure 10: *Measurement of F_2 as a function of Q^2 in bins of fixed x between $x = 0.008$ and $x = 0.08$. The H1 preliminary data are compared to the NMC data, and to the H1 NLO QCD fit.*

In Fig. 9 the H1 data are shown at fixed x as a function of Q^2 and compared to the QCD fit. Also included in the plot are the high Q^2 preliminary measurements at high Q^2 on the 1994-97 data which will be described below. A good description of the data by the NLO DGLAP fit is realized over more than four orders of magnitude in x and Q^2. The figure shows clearly the famous scaling pattern at $x \simeq 0.1$ and the scaling violations which becomes stronger when going to low x due to the larger gluon radiation.

In Fig. 10 an enlargement of the same plot is made in the region where scaling is starting to be realized, around $x \simeq 0.1$. On this plot we can observe that the precision on F_2 at HERA is now comparable to the one obtained at fixed target experiments (a few percent), and that a good agreement between all these measurements using very different techniques can be observed. With the extension to high Q^2 brought by HERA, the scaling properties at $x \simeq 0.1$ are now observed up to $Q^2 = 5000$ GeV^2.

6 Extraction of F_L from the Cross-Sections at High y

The cross-section measurement at low Q^2 and at y close to 1 is particularly difficult at HERA since it requires the identification of the scattered positron having a few GeV in energy, while the photoproduction events which are occurring at a much higher rate often produce fake electrons in this energy range. At these low energies the usual trigger requirement of energy deposited in the calorimeter has to be complemented by a track requirement in order to get rid of beam induced background. Moreover, at low energies, even for $Q^2 \simeq 10$ GeV^2, the positron is scattered at relatively low angles ($\theta_e \simeq 160°$). Therefore at low Q^2 and at the largest y, the track of the positron is in the acceptance of the tracking system. This permits the subtraction of the photoproduction background using techniques based on the measured charge of these tracks.[25] Since at low energies the positron has less energy than the hadronic final state which is also scattered backwards, the positron identification procedure has also to be changed. Thus the unique features of the high y analysis are a modified positron identification and the requirement of a track with correct charge pointing to the calorimeter cluster.

The result for the measured DIS reduced cross-section for Q^2 between 12 and 35 GeV^2 is shown in Fig. 11 which compares the published 1994 data[28] with the preliminary 1996[29] and 1997[25] data. The reduced cross-section is defined as

$$\tilde{\sigma} = \frac{1}{\kappa}\frac{d^2\sigma}{dxdQ^2} = F_2 - \frac{y^2}{Y_+}F_L \text{ with } \kappa = \frac{2\pi\alpha^2 Y_+}{Q^4 x} \text{ and } Y_+ = 1 + (1-y)^2 \qquad (5)$$

when the Z^0 exchange is neglected. The error bars comprise both statistical and systematic errors added in quadrature. Both cross-section measurements agree well. For four Q^2 points the y range was extended with measurements up to $y = 0.82$ which considerably enhances the sensitivity to F_L.

Figure 11 shows also calculations of the cross section using the QCD fit to F_2, described in Section 4, and three different assumptions on the longitudinal structure function F_L. The measured cross-section is in agreement with the NLO QCD calcula-

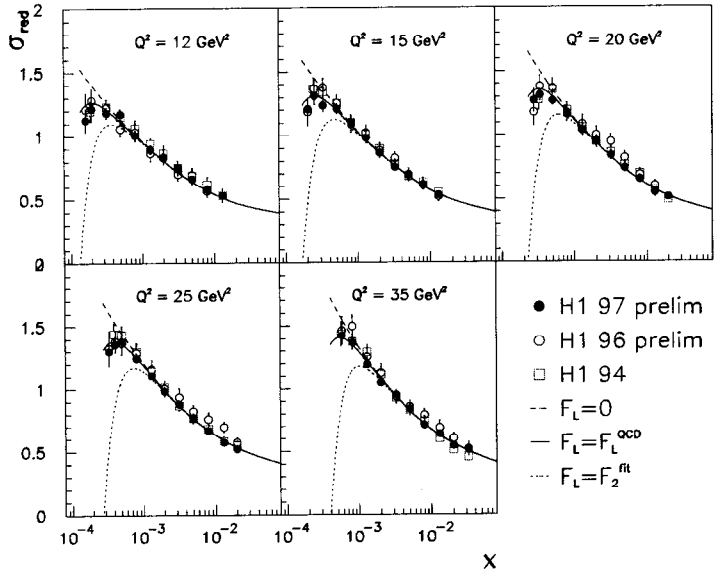

Figure 11: *Measurement of the reduced DIS cross-section at low Q^2. Closed circles: H1 1997 preliminary measurement. Open circles: H1 1996 preliminary measurement. Open squares: H1 data from the 1994 run[28] taken with a former backward setup. The lines use the QCD calculation of F_2 and of F_L (solid line) or the extreme assumptions $F_L = F_2$ (dotted line) and $F_L = 0$ (dashed line). The largest y value is 0.82.*

tion apart from large y, for $12 \leq Q^2 \leq 25$ GeV^2, where the measured points tend to be lower than the QCD lines (solid lines in Fig. 11).

F_L is then determined at $y = 0.68, 0.82$ by subtracting to the reduced cross-section, the extrapolated value of F_2 as predicted by a QCD fit to the data at lower y (< 0.35), on which the influence of F_L is negligible.

$$F_L = \frac{Y_+}{y^2}\left(F_2^{fit} - \frac{1}{\kappa}\frac{d^2\sigma^{exp}}{dxdQ^2}\right). \tag{6}$$

These results are shown and compared to another determination of F_L based on the measured $\partial\tilde{\sigma}/\partial\log y$ derivatives, in the next two sections.

6.1 Determining F_L using $\partial\tilde{\sigma}/\partial \ln y$

The cross-sections were used to measure the derivatives $\partial\tilde{\sigma}/\partial\log y$ at fixed Q^2 in the whole y range. This derivative is defined at fixed Q^2 as:

$$\frac{\partial\tilde{\sigma}}{\partial \ln y} = -\frac{\partial F_2}{\partial \ln x} - F_L \cdot 2y^2 \cdot \frac{2-y}{Y_+^2} + \frac{\partial F_L}{\partial \ln x}\cdot\frac{y^2}{Y_+}. \tag{7}$$

In Fig. 12 the cross-section derivative measurements are compared with the NLO QCD calculation using different assumptions on F_L. The derivative is seen to be sensitive to the longitudinal structure function. For $y \to 1$ the cross-section derivative tends to the limit $-\frac{\partial F_2}{\partial \ln x} - 2\cdot F_L$ with a negligible contribution from the derivative of F_L. This is in contrast to the F_L influence on the non-differentiated cross-section $\tilde{\sigma}$, see Fig. 11, where the contribution of F_2 dominates for all y and thus has to be controlled with high precision.

The measurement of $\frac{\partial\tilde{\sigma}}{\partial \ln y}$ can be used to determine F_L in a new way. Assuming that $\partial F_2/\partial \ln y = A \ln y + B$, straight line fits were made to $\partial\tilde{\sigma}/\partial \ln y$ in Q^2 bins on the measured points at $y < 0.2$. The extrapolation of those fits are taken to represent the contribution of F_2 at high y, and the uncertainties of the straight line fit are included in the systematic error. The small contribution of $\frac{\partial F_L}{\partial \ln y}$ to the derivative is corrected for using NLO QCD. This new method gives access to a lower Q^2 than the subtraction method seen above, since no QCD extrapolation at low x and low Q^2 are needed here.

6.2 Results on the Longitudinal Structure Function F_L

The results of these two methods of F_L determination are shown in Fig. 13 and they are compared to the NLO QCD expectation. The subtraction method ($\bullet$) and the derivative method ($\star$) give consistent results in good agreement with QCD. These two methods use the same data but different characteristics of the F_2 and F_L behavior. Note however that the systematic errors of the points at the same y are strongly correlated, implying that the tendency of the data points at $y = 0.82$ to lie above the QCD expectation is not significant.

In the future F_L will be measured directly by changing beam energies.

7 The Charm Contribution to F_2

The F_2 structure function is related to the quark and gluon densities of the proton. Thus, beyond the inclusive study of the proton structure it is also possible to pin down

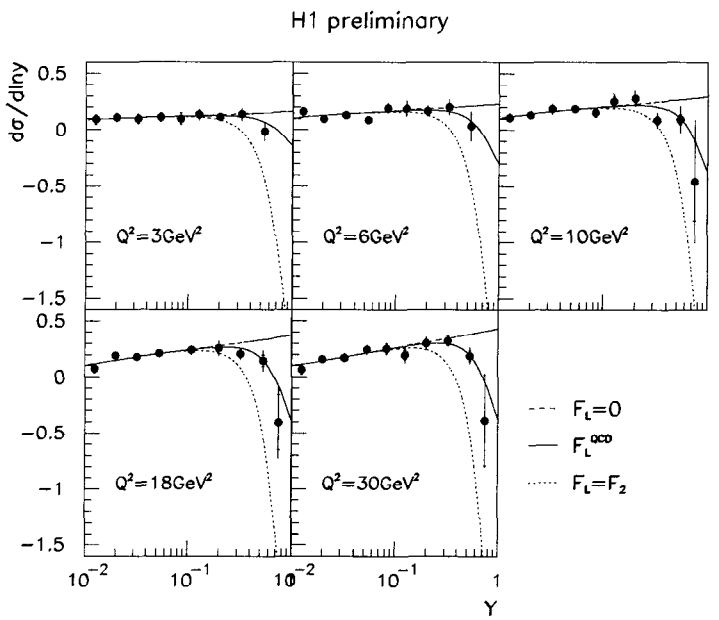

Figure 12: *Measurement of $\partial\tilde{\sigma}/\partial \ln y$ at fixed Q^2 using the1997 H1 data. The influence of F_L on this measurement is displayed by the curves which give the QCD expectation ($F_L = F_L^{QCD}$) and two extreme cases ($F_L = 0$), ($F_L = F_2$).*

exclusively the different contributions arising from the gluon or a given quark flavor, by separating the contribution from the light quarks, u, d, and s from the contribution of heavy quarks, in particular the charm contribution which is accessible with the present statistics in the kinematic domain of HERA.

The charm production in DIS occurs predominantly via photon-gluon fusion (BGF), which has been calculated analytically in NLO.[30] Other contributions to the charm production arising from diffractive heavy flavor production,[31] from the scattering of the virtual photon off a charm sea quark (flavor excitation process),[32] from charmed hadron production after the decay of b flavored hadrons[33] or from the production of $c\bar{c}$ in fragmentation,[34] are expected to have much smaller cross sections than BGF. The

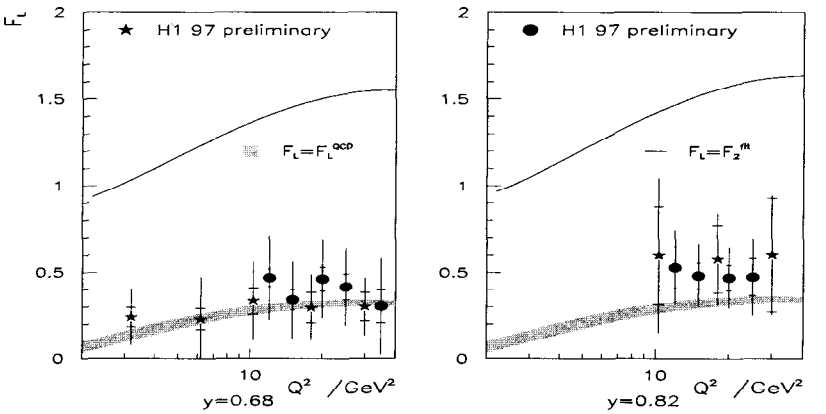

Figure 13: *Determination of the longitudinal structure function F_L using the two methods described in the text. The two determinations use the same data set. The narrow band represents the uncertainty range of F_L when calculated using the gluon and quark distributions determined with the H1 NLO QCD.*

possible contribution of intrinsic charm would give rise to charm production at large x,[35,32] and is currently beyond reach at HERA. Figure 14 illustrates the contribution from light quarks to the total F_2, as obtained by a NLO QCD fit[4] to the NMC and ZEUS F_2 measurements in bins of x as a function of Q^2. At high x, approaching the valence quark region, no contribution from the heavy quark flavors is expected, as well as at low Q^2, where the production of heavy flavors is suppressed due to their heavy mass. However at low x and relatively high Q^2, the charm contribution to F_2 amounts, according to the QCD fit results, to up to 25%.

In the NLO QCD fit programs used by H1 and ZEUS, the charm contribution is generated dynamically from BGF,[36,37] where both the renormalization and the factorization scales are taken as $\mu = \sqrt{Q^2 + 4m_c^2}$. The largest uncertainties in this calculation are related to that of the charm quark mass to which a typical uncertainty of about 30% is assigned. The direct measurement of the charm contribution to F_2 therefore allows for a test of this approach, and the close relation between BGF and the gluon density of the proton provides another independent way to measure the gluon density via the charm production.

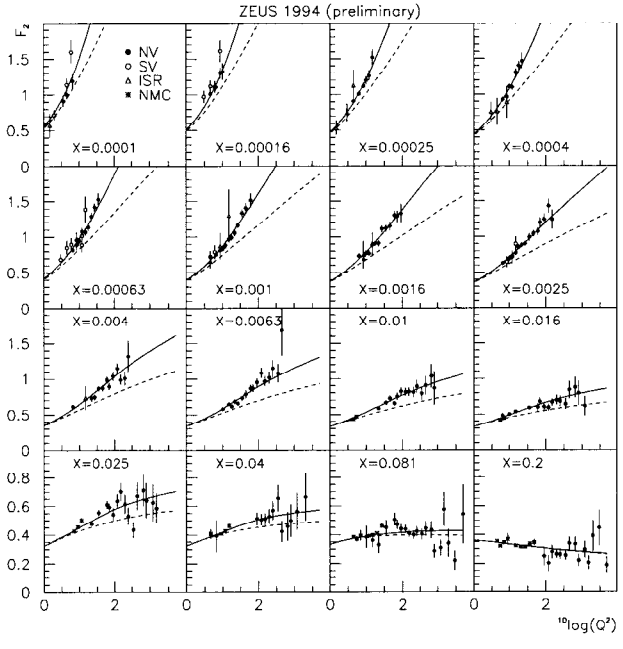

Figure 14: *The contribution from the charm quark to the inclusive F_2 from NLO-QCD fit. The full line corresponds to $F_2 = F_2^{u,d,s} + F_2^c$, whereas the dashed line accounts only for the contribution from the light quarks $F_2 = F_2^{u,d,s}$. The datasets used in the fit correpond to the ZEUS measurements on '94 data at nominal vertex (NV)[4] and shifted vertex (SV) events with initial state photon radiation (ISR)[12] and to the NMC data.[45]*

7.1 Charm in DIS

So far two ways to tag charm in DIS were explored at HERA: the open charm production of D^* or D^0 mesons,[38,39] and the identification of electrons from semileptonic charm decays.[40] The initial DIS sample reaches from $1 < Q^2 < 600$ GeV^2 and $0.02 < y < 0.7$. The D^* mesons are reconstructed using the decay

$$D^{*+} \to D^0\pi^+ \to (K^-\pi^+)\pi^+ + c.c., \tag{8}$$

which has a branching ratio of 2.62%.[41] The decay products are detected in the central trackers leading to an acceptance of $|\eta| < 1.5$ and of $1.5 < p_T(D^*) < 15$ GeV. No particle identification is performed and therefore the tracks assigned to the charged kaon and pion are required to produce an invariant mass $M(K\pi)$ between 1.80–1.92 GeV and a difference $M(K\pi\pi) - M(K\pi)$ between 143–148 MeV.

From the number of events obtained the derived total cross-section is

$$\sigma(ep \to eD^*X) = 8.55 \pm 0.40^{+0.30}_{-0.24}\ \text{nb}. \tag{9}$$

The differential cross-sections as functions of Q^2, x, W, $p_T(D^*)$, $\eta(D^*)$, and $x(D^*)$ are shown in Fig. 15. The measurement is compared to the prediction using the Monte Carlo-like program HVQDIS,[42] where the charm production is calclulated from BGF and the obtained production cross-section is convoluted with the Peterson fragmentation function[43] in order to obtain the visible D^* cross-section. The light parton distributions are taken from the GRV94 HO parton distributions. The error band represents a variation in the charm mass between 1.2 and 1.6 GeV and a good agreement of this "massive" NLO pQCD calculation with the measurement is observed, except for some small deviations at high-η and low-x of the D^* meson.

A component of direct electrons in jets can be ascribed to the semileptonic decay of charmed hadrons. In order to identify the electrons, the dE/dx measurement from the central tracking system is used. Supplementary cuts on the shower shape variables of calorimetric measurement associated to these tracks allow for a rejection of the charged pion background, and algorithms on mutually tangential tracks differentiate the electrons from photon conversion from the prompt electrons from the signal. The electron tracks identified by this procedure are only considered for $p > 1.2$ GeV and in the central tracking system with $0.65 < \theta < 2.5$. Acceptance corrections for these cuts as well as trigger and detection efficiencies are obtained from detailed Monte Carlo studies. Furthermore the inclusive $c \to e$ branching ratio $9.8 \pm 0.9 \pm^{0.6}_{0.5}$ % as measured by ARGUS[44] is applied in order to unfold the cross-section.

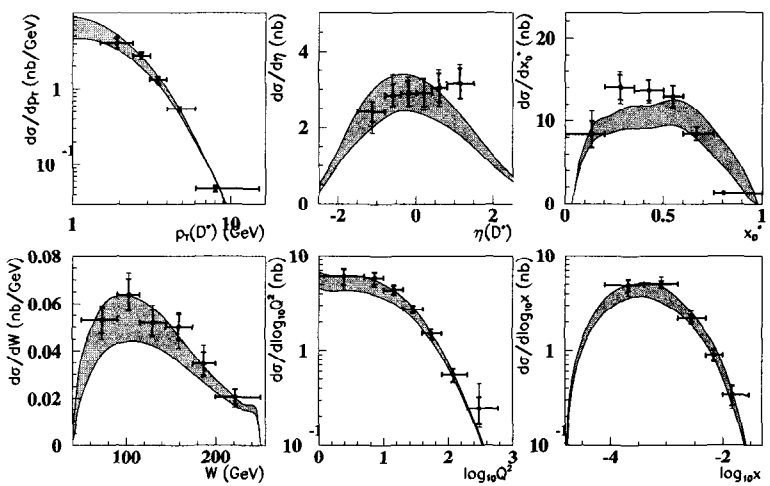

Figure 15: *Differential D^* cross-sections as functions of $\log Q^2$ (a), $\log x$ (b), W (c), $p_T(D^*)$ (d), $\eta(D^*$ (e), and $x(D^*)$ (f). The data points are compared to a NLO QCD fit, where the error band corresponds to a variation in the charm mass between 1.2 GeV (upper boundary) and 1.6 GeV (lower boundary).*

7.2 Measurement of F_2^c

The charm structure function F_2^c is related to the differential cross-section for $c\bar{c}$ production by

$$\frac{d^2\sigma_{c\bar{c}X}}{dx\,dQ^2} = \frac{2\pi\alpha^2}{xQ^4}[1+(1-y)^2]F_2^c(x,Q^2) \qquad (10)$$

considering in the given kinematic range only one photon exchange and neglecting an F_L^c contribution, which is estimated from NLO predictions to be lower than 1% in the measured Q^2, y region. For the extraction of F_2^c the cross-sections measured in a restricted p_T and η region are extrapolated to the full phase space using the HVQDIS program. Typical extrapolation factors are between 4 at low Q^2 and 1.5 at high Q^2. These extrapolated cross-sections are then translated into $c\bar{c}$ cross-sections using the constant hadronization fraction of charm to D^{*+}, $f(c \to D^{*+}) = 0.222$.

Figure 16 is showing the preliminary results of the F_2^c measurement in various bins of Q^2 as a function of x for the D^* and the semileptonic analyses on datasets taken

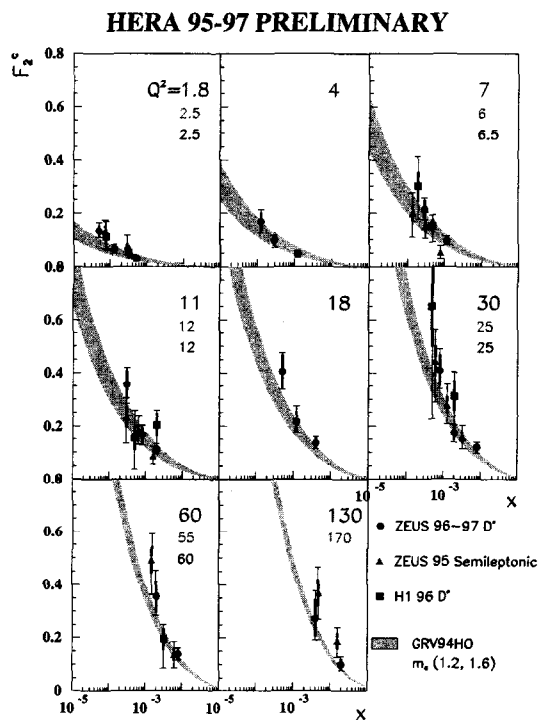

Figure 16: *F_2^c from D^* and semileptonic decays compared to the prediction from GRV94HO with a variation of the charm mass between 1.2 and 1.6 GeV.*

during the '95, '96, and/or '97 running periods. The results from the different analysis methods are in good agreement with a precision of about 15–20 %, which is still largely dominated by the statistics, but significantly more precise than the earlier measurements. The behavior of F_2^c shows a steep rise towards low x, which can be understood as being directly correlated to the steep rise of the gluon density established by the former inclusive measurements of F_2 at low x. The indirect prediction from perturbative QCD of the charm contribution is in good agreement with the direct measurements.

8 The Gluon Density of the Proton

One of the major results of the first years of the running of HERA was to establish the steep rise of the proton structure function at low x and its relation to the increase of the gluon density, which is extracted from NLO QCD fits to the structure function measurement. But the gluon density can also be extracted from processes invoking photon-gluon fusion (BGF), like the charm production, giving a cross check of the global measurement and access to different kinematic ranges.

8.1 The Gluon Density from NLO QCD Fit

The NLO QCD fits used to extract the gluon densities from the inclusive F_2 measurements are described in section 4.1. As the HERA data do not constrain the high x region, proton and deuteron structure function data from NMC[45] and BCDMS[60] were included in the fit.

Figure 17 shows the gluon densities obtained by the H1[46] and the ZEUS[24] fits at $Q^2 = 20\text{GeV}^2$. Both results are in good agreement and show a steep rise of $xg(x)$ for decreasing x, which is mainly due to the asymptotic behavior in $\log 1/x$ of the solutions to the DGLAP equations. The error bands shown take into account the statistical errors, a full treatment of the correlated systematic errors and possible variations of α_S and of the charm mass. The precision obtained for the gluon density at $x \sim 5 \cdot 10^{-4}$ is about 15%. The results from the HERA experiments allow for a smooth transition towards the results from NMC in the high x domain and are consistent with the gluon density of the MRSR1[47] and CTEQ4M[48] parametrizations obtained from fits to a wider number of datasets. The gluon density from the GRV[16] parametrization gives a somewhat higher result, which is understandable since it assumes a lower α_S value than the other fits.

The non-singlet quark momentum distribution $xq_{NS} = \sum_{i=1}^{n_f}(xq_i - x\bar{q}_i) = xu_{val} + xd_{val}$, which expresses the sum of the valence quark densities, evolves independently of the gluon distribution, while the singlet quark distribution $x\Sigma = \sum_{i=1}^{n_f}(xq_i + x\bar{q}_i)$ is coupled to the gluon distribution, since at small values of x, $x\Sigma$ is dominated by the contribution of the sea $q\bar{q}$ pairs.

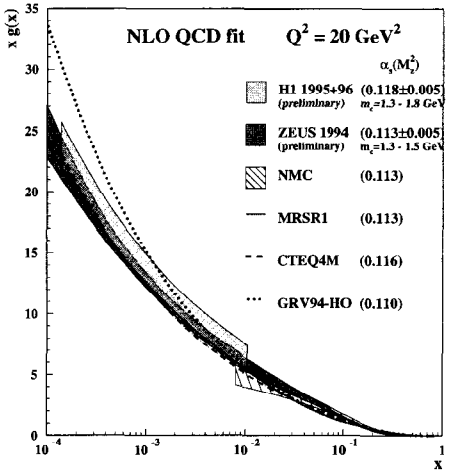

Figure 17: *The gluon density of the proton as obtained from NLO order fit to the inclusive F_2 measurements at $Q^2 = 20$ GeV^2 by the H1 and ZEUS collaborations compared to the results of the NMC Collaboration at high x and results from the global analyses by MRSR and CTEQ as well as the prediction from GRV94. The α_s values used in the fits are quoted between brackets.*

Figure 18 is comparing the singlet quark distribution with the gluon distribution at $Q^2 = 20$ GeV^2, $Q^2 = 7$ GeV^2, and $Q^2 = 1$ GeV^2. In the two higher Q^2 bins, the xg shows a steeper rise at low x than the sea quark densities. At $Q^2 = 1$ GeV^2, the gluon density shows an almost flat behavior at $Q^2 = 1$ GeV^2, indeed compatible with 0, while $x\Sigma$ is still slightly rising. This difference in behavior may indicate a difference in the dynamics when approaching the transition region, at $Q^2 \approx 1$ GeV^2, from perturbative to non-perturbative QCD.

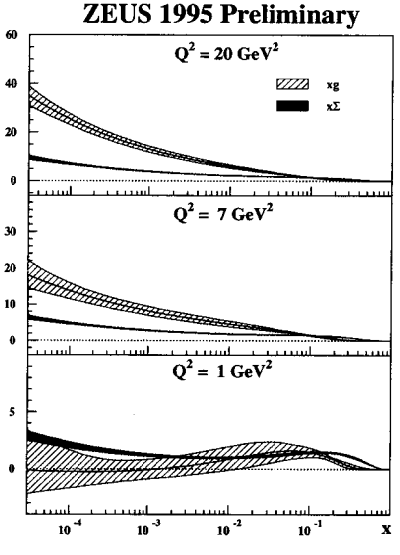

Figure 18: *The quark singlet momentum distribution $x\Sigma$ (shaded) and the gluon momentum distribution $xg(x)$ (hatched) as a function of x at different values of Q^2.*

8.2 The Gluon Density from the Charm

In a similar way to how the F_2^c contribution is extracted from the open charm production, the unfolding can be also done directly for the gluon density.[49] This is possible, not only in DIS, but also from D^* events in photoproduction, where $Q^2 \simeq 0$, using the FMNR program[50] to calculate the cross-sections. For the unfolding procedure, the gluon momentum fraction x_g is determined from the momentum carried by the D^* meson using an iterative procedure. Each value of x_g corresponds to a different scale, and the results is shown in Fig. 19 at the average scale $\mu^2 = 4m_c^2 + \langle Q \rangle^2 = 25$ GeV^2.

The results of both D^* analyses are in good agreement, and are consistent at low x with the determination of the gluon density from the QCD fit to F_2. The measured values are also well described by the CTEQ4F3[48] parametrization, both at low and high x.

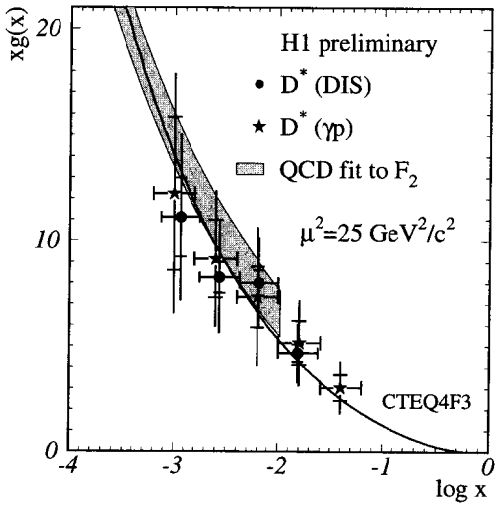

Figure 19: *The gluon density obtained from the D^* production in DIS and photoproduction compared to the results of the gluon extraction from the inclusive F_2 measurement at $\mu^2 = 25$ GeV^2 and the CTEQ4F3 parametrization.*

9 DIS Events at High Q^2

With the increased luminosity produced by HERA during the past four years, the high Q^2 region, *i.e.*, Q^2 typically above 100 GeV^2, became accessible for precision measurements, for the observation of electroweak effects in ep scattering and for the exploration of the very high Q^2 region and the search for exotic particles.[51] In Fig. 20b is shown a high Q^2 Neutral Current event detected in the ZEUS detector, in which the electron is backscattered in the forward direction. In Fig. 20a is shown a charged current event in the H1 detector, in which the outgoing neutrino escapes undetected, leading to a large missing transverse momentum.

From 1994 until 1997, HERA was colliding positrons off protons. At low Q^2 the e^-p and e^+p cross-sections are identical, but at high Q^2 the increasing influence of the weak contributions gives rise to a destructive interference of the electromagnetic and

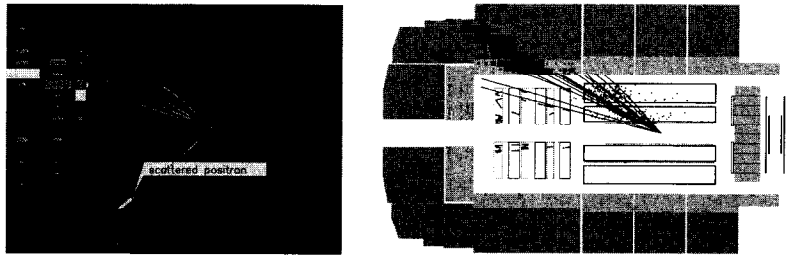

Figure 20: *Neutral (left) and Charged (right) Current events seen in the ZEUS and in the H1 detectors. The incident positron comes from the left, the proton from the right.*

the weak contribution and decreases the e^+p cross-section compared to the e^-p one.[5,6] The comparison of Neutral and Charged Current cross-sections as functions of Q^2 as shown in Fig. 21 displays their similar behavior at $Q^2 > 10000$ GeV^2, a region where the weak contribution becomes important, whereas at lower Q^2, the NC cross-section is rising steeply, contrarily to the CC cross-section, which increases mildly at lower Q^2. The remaining differences at high Q^2 are due to the weak coupling to the different quark flavors. At very high Q^2, above 15000 GeV^2, is the region where the excess of events was reported[52,53] on the 1994 to 1996 data. This excess is still visible, but has lowered in significance after including the 1997 data.[54,55]

9.1 Neutral Current Cross-Sections

The NC cross-section for unpolarized e^+p scattering can be written as a linear combination of the F_2, F_3, and F_L structure functions:

$$\frac{d^2\sigma^{e^+p}}{dx\,dQ^2} = \frac{2\pi\alpha^2}{xQ^4}\left[Y_+F_2(x,Q^2) - y^2F_L(x,Q^2) - Y_-xF_3(x,Q^2)\right]. \qquad (11)$$

In this equation α is the fine structure constant, and the helicity dependence of the electroweak interactions is contained in the function Y defined as $Y_\pm(y) = 1 \pm (1-y)^2$. The generalized structure function F_2 can be decomposed as

$$F_2 = F_2^{em} + \frac{Q^2}{(Q^2+M_Z^2)}F_2^{int} + \frac{Q^4}{(Q^2+M_Z^2)^2}F_2^{wk} = F_2^{em}(1+\delta_Z) \qquad (12)$$

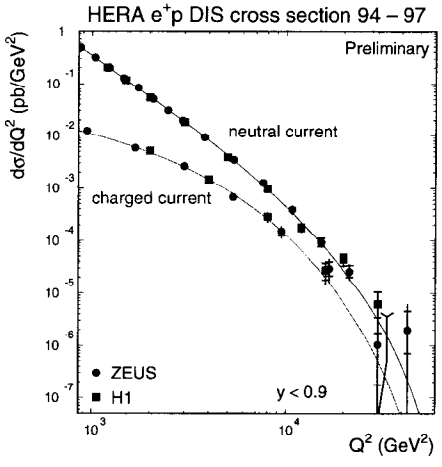

Figure 21: *Single differential cross-section as a function of Q^2 for Neutral and Charged Currents.*

where F_2^{em} contains the contribution from the pure photon exchange, F_2^{wk} the one of the Z^0 exchange, and F_2^{int} the γZ^0 interference. The reduced cross-section is defined in eq. 5 as

$$\tilde{\sigma}(e^+p) \equiv \frac{xQ^4}{2\pi\alpha^2}\frac{1}{Y_+}\frac{\mathrm{d}^2\sigma}{\mathrm{d}x\mathrm{d}Q^2} \qquad (13)$$

and can be written as $F_2^{em}(1+\delta_Z-\delta_3-\delta_L)$ with δ_Z, δ_3, and δ_L being small at low Q^2. The contributions from F_2^{em} and from F_2 to the reduced NC cross-section for $Q^2 \geq 3000$ GeV^2 are shown in Fig. 22, which depicts the effect of the γZ destructive interference in e^+p collisions, which is most important at high y. The contribution from $\delta_Z - \delta_3$ is below 1% at $Q^2 < 1500$ GeV^2 and about 10% at $Q^2 = 5000$GeV^2 and $x = 0.08$. The influence of the longitudinal structure function δ_L is negligible at $y < 0.5$ and up to 5% at $y = 0.9$. At $Q^2 \geq 15000$ GeV^2 no structure function has a dominant contribution. All the NC cross-sections presented have been corrected for QED radiation from the lepton line, whereas the radiation from the quark line can be safely neglected.

The preliminary results from H1 on the reduced NC cross-section are shown in Fig. 23 for 200 GeV$^2 \leq$ Q$^2 \leq$ 30000 GeV^2 and $0.005 \leq x \leq 0.65$. The NLO QCD fit gives a good description of the data in the whole Q^2 and x range. Above $Q^2 = 1000$

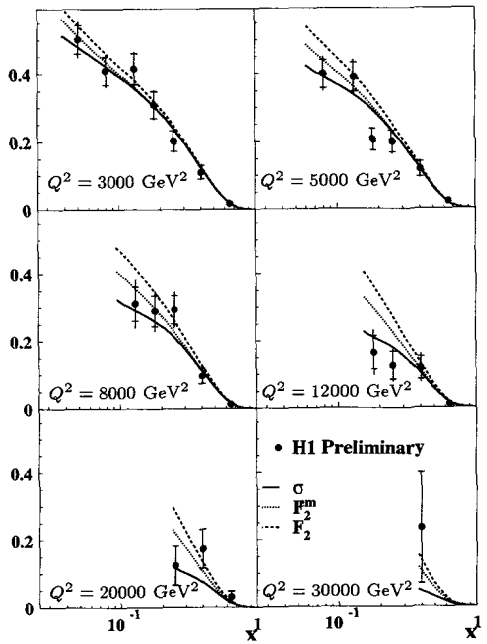

Figure 22: *The reduced NC cross-section for $Q^2 \geq 3000$ GeV^2. Indicated are the contributions from the electromagnetic F_2^{em} and the generalized F_2 as obtained in the NLO QCD fit to the data.*

GeV^2, the statistical error grows typically to 5-15% and dominates the total error. The total error (quadratic sum of the systematic and of the statistical error) is below 10% at $Q^2 \lesssim 1000$ GeV^2.

In Fig. 24 is shown the ZEUS preliminary F_2 measurement on the 1996-1997 data at $Q^2 \geq 800$ GeV^2 which is compared to the previous measurement on the 1994 data done on statistics about ten times lower. The new measurement extends in range the previous one and improves its precision.

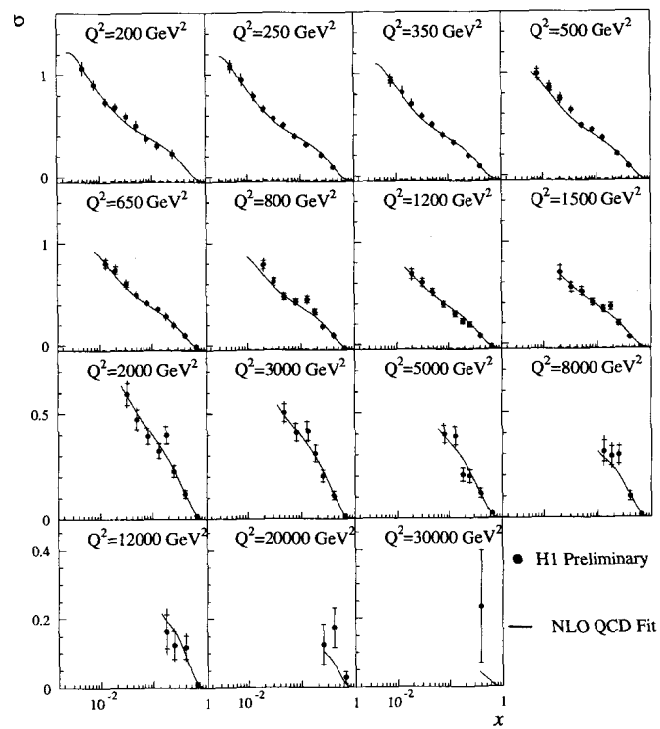

Figure 23: *Preliminary 1994-1997 H1 results on the reduced NC cross-section compared to the NLO QCD fit.*

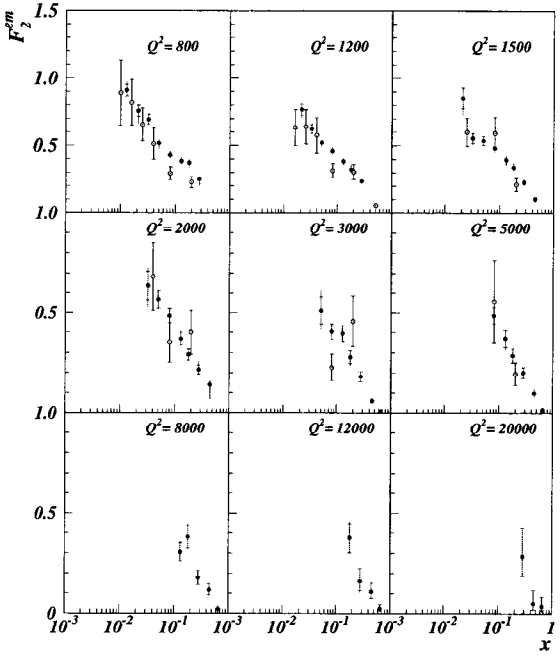

Figure 24: *ZEUS preliminary results (1996-1997 data) on F_2 measured at high Q^2 compared to the ZEUS 1994 measurement.*

9.2 The Weak Contribution to the NC Cross-Section

The effect of the γZ interference is visible at HERA for the first time, as can be shown on the NC cross-section $d\sigma/dx$. In Fig. 25 is shown the $d\sigma/dx$ cross-section at $Q^2 > 1000$ GeV^2. The measurement extends from $1.3 \cdot 10^{-2}$ to 0.65. The maximum of the distribution is obtained at $\approx 2 \cdot 10^{-2}$, *i.e.*, at this low Q^2, the cross-section is still dominated by low x, "sea" partons (the sharp drop of the cross-section at $x < 2 \cdot 10^{-2}$ comes from the kinematic inaccessibility of this region at high Q^2). No difference in the prediction is observed with respect to the Standard Model if only γ exchange is taken into account. In contrast, at $Q^2 > 10000$ GeV^2 the two predictions are significantly different, and the data which have now their maximum in the valence region ($x \approx 0.2$),

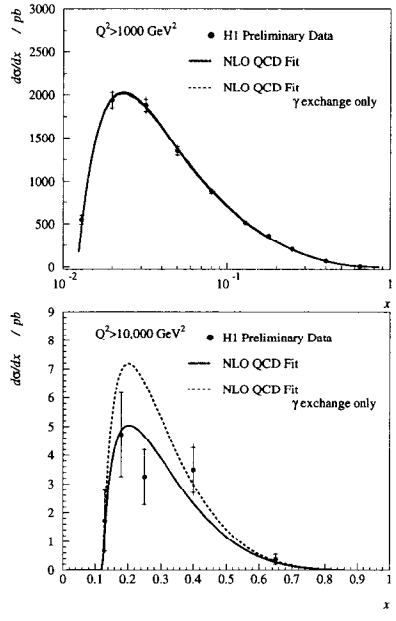

Figure 25: *The neutral current cross-section $d\sigma/dx$ at high Q^2 compared with the Standard Model prediction and with the prediction when the coupling to the Z boson is not taken into account.*

agree with the Standard Model prediction and disagree at the three standard deviation level if only γ exchange is taken into account.

9.3 Reduced Cross-Section at High x

In Fig. 26 the emphasis is put on the high x region, and the reduced cross-section is shown as a function of Q^2 at fixed values of x between $x = 0.07$ and $x = 0.65$. At $x = 0.45$ some excess of the cross-section over the Standard Model prediction is visible for the highest Q^2 values, which corresponds to the accumulation of events around an inclusive invariant mass of the lepton quark system of about 200 GeV, and which was already pointed out in the 1994 to 1996 data.[52] The significance of this excess has decreased with the enhanced statistics which include the 1997 data.

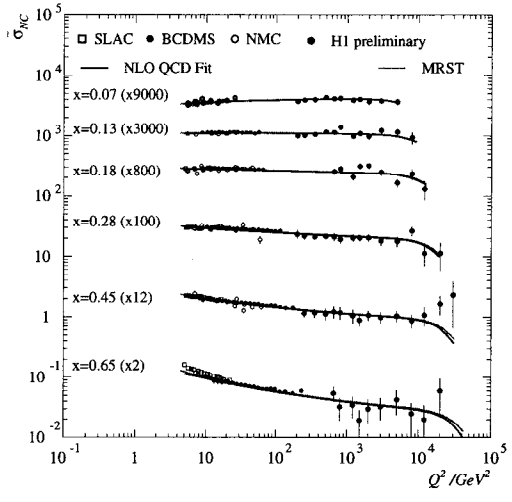

Figure 26: *The reduced neutral current cross-section at high x compared with Standard Model predictions from MRST and the H1 NLO QCD fit. The error bars represent the total error of the measurements.*

The cross-section is compared to the MRST[59] parton density and the NLO QCD fit. At the lowest x value of 0.07, both parameterizations are in good agreement, but at higher x the new data, which are included in the QCD fit, lower the prediction from the fit by up to 5%. The direct comparison with the BCDMS measurement[60] shows the same trend: from $x = 0.28$ up to $x = 0.65$, the H1 data are slightly below the extrapolation obtained from the BCDMS data.

9.4 Charged Current Cross-Sections

The Born double differential CC cross-section can be expressed as in the NC case

$$\left(\frac{d^2\sigma_{CC}}{dx\, dQ^2}\right)_{Born} = \frac{G_F^2}{2\pi x} \cdot \left(\frac{M_W^2}{M_W^2 + Q^2}\right)^2 \cdot \phi_{CC}(x, Q^2) \qquad (14)$$

with G_F being the Fermi coupling constant, M_W the mass of the W boson, and $\phi_{CC}(x, Q^2)$ the CC structure function term. In the special case of leading order QCD, and neglecting the effect of quark mixing, this cross-section is related to the quark parton densities (xu, xd, xs, xc) which are functions of x and Q^2:

$$\left(\frac{d^2\sigma_{CC}}{dxdQ^2}\right)_{LO} = \frac{G_F^2}{2\pi}\left(\frac{M_W^2}{M_W^2 + Q^2}\right)^2 \left((\bar{u} + \bar{c}) + (1-y)^2(d+s)\right). \qquad (15)$$

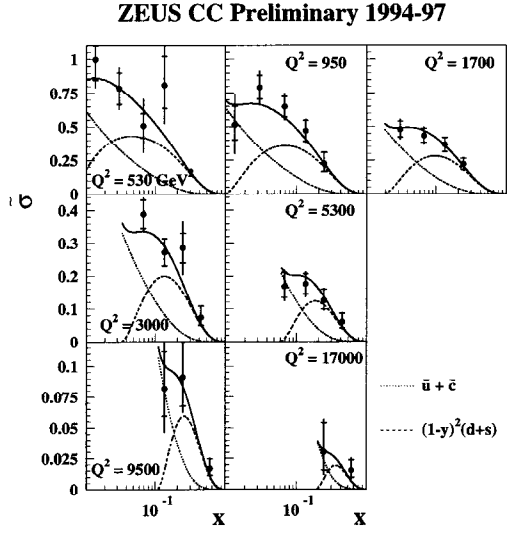

Figure 27: *The reduced charged current cross-section as a function of x for different Q^2 compared with the Standard Model prediction (using CTEQ4D parton distributions) and the xd contribution to it.*

The reduced charged current cross-section is defined in analogy with the NC one:

$$\tilde{\sigma}_{CC}(x, Q^2) \equiv \frac{x \cdot 2\pi}{G_F^2}\left(\frac{M_W^2 + Q^2}{M_W^2}\right)^2 \frac{d^2\sigma_{CC}}{dxdQ^2}. \qquad (16)$$

Note that with this definition, apart for the small weak radiative corrections which have not been applied, the CC reduced cross-section is equal to the structure function term, while the NC reduced cross-section has an extra $1/Y_+$ term.

The double differential CC cross-section has been measured for the first time at high Q^2 by H1 and ZEUS. The ZEUS preliminary results are displayed in Fig. 27. They are

still largely dominated by the statistical error. The most important systematic error is the uncertainty on the energy scale of the hadronic final state. Within these errors, the measurement is in good agreement with the predicted cross-section from the Standard Model using the MRST[59] parton distributions. Also shown is the contribution to the cross-section of the term $(1-y)^2 x(d+s)$ which is dominated in the Standard Model by the d valence quark at high x. The strong suppression of the d and s contributions

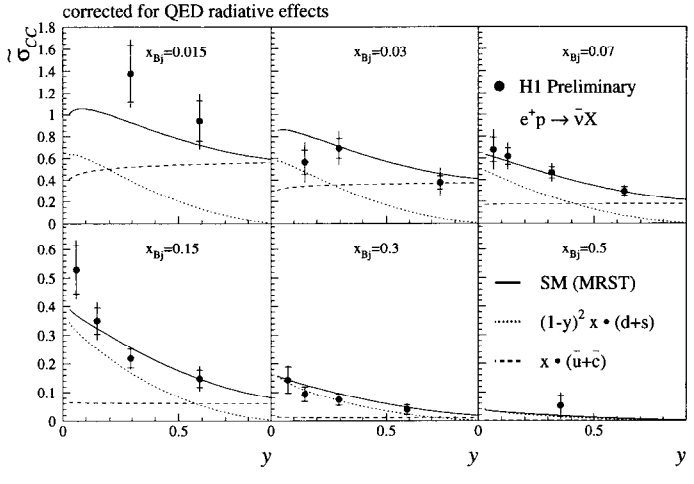

Figure 28: *The reduced charged current cross-section as a function of y for different values of x (lower plot) compared with the Standard Model prediction (using MRST parton distributions) and the $(d+s)$ and sea antiquarks' contribution to it.*

in the double differential CC cross-section at high y due to the $(1-y)^2$ term, and the small contribution of the sea quarks at high x, are better studied when replotting the reduced cross-section at fixed x as a function of y, as can be seen in Fig. 28. The relative contribution given by the MRST parametrization are also shown. As expected, the reduced cross-section grows at low y, because the $(1-y)^2$ term increases towards one, and it grows at low x since the sea quark contribution increases in this domain. At $x = 0.3$, the shape of the measured distribution, which decreases quickly towards zero, indicates that the sea quark contribution is indeed small at large x.

9.5 The Propagator Mass M_W

In the Standard Model the CC cross-section is directly sensitive to the Fermi coupling constant (G_F) and the W mass (M_W). It is visible from the leading order CC cross-section formula that the constraint on M_W comes from the propagator factor, $[(M_W^p)^2/(Q^2+(M_W^p)^2)]^2$, where in the SM, the propagator mass $M_W^p \equiv M_W$. Since CC interactions arise from the t channel exchange of a virtual W boson, the value of M_W^p extracted from the propagator factor can be interpreted as a direct measurement of the W mass in the spacelike regime. It is a crucial test of the universality of the Standard Model to compare such a measurement with timelike and indirect determinations from other experiments.

In order to construct a fit of the CC cross-section that is sensitive only to the value of M_W^p from the propagator term, the Standard Model expectation for the CC cross-section is obtained in which M_W^p is allowed to vary, and is decoupled from the value of M_W entering the theoretical expectation for $G_F(\alpha, M_W, M_Z, M_{top}, M_H)$.

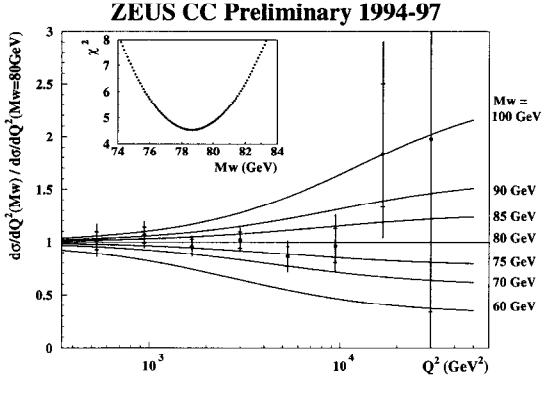

Figure 29: *The points show the ratio of the measured cross-section to the Standard Model prediction. The solid curves show the expected deviations of the cross-section from the nominal $M_W = 80$ GeV scenario for various indicated values of M_W. Inset is the χ^2 fit of the data to the Standard Model plotted againt M_W.*

In Fig. 29 is shown the result of the ZEUS fit, where the ratio of $d\sigma(M_W)/dQ^2$ to $d\sigma(M_W = 80\ \text{GeV})/\text{dQ}^2$ is plotted as a function of Q^2 together with the χ^2 of the

fit to the ZEUS cross-section measurement, as a function of the propagator mass. The propagator mass results from the HERA[56,58] experiments are

$$81.2\ ^{\pm 3.3 \pm 4.3}\ \text{GeV for the H1 experiment} \tag{17}$$

$$78.6\ ^{+2.5+3.3}_{-2.4-3.0}\ \text{GeV for the ZEUS experiment.} \tag{18}$$

Both results are in agreement with the world average $M_W = 80.41 \pm 0.10$ GeV.[41]

9.6 Comparison of the NC and CC Cross-Sections at High x

At $x \geq 0.3$ the CC cross-section is largely dominated by the d valence quark. The comparison in the high x domain of the NC structure function term (*i.e.*, $Y_+\tilde{\sigma}_{NC}$) with the CC one (*i.e.*, $\tilde{\sigma}_{CC}$) as shown in Fig. 30, in a region in which the γZ interference term is still small ($Q^2 \lesssim 5000$ GeV^2), gives direct information on the relative size of u_v and d_v at high Q^2. From the 2000 and 4000 GeV^2 points of Fig. 30, we can observe that the u valence quark distribution is between 1.5 to 3 times larger than the d at $x = 0.3$.[56]

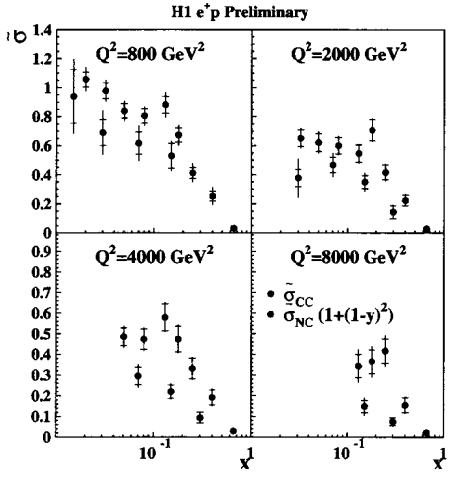

Figure 30: *Comparison of the structure function terms of the NC and CC double differential cross-sections (i.e., of $Y_+\tilde{\sigma}_{NC}$ and $\tilde{\sigma}_{CC}$) as a function of x in bins of Q^2.*

10 Summary

In its first years of operation, HERA has been testing the Standard Model, in particular QCD and the structure of the proton, in new kinematic domains. A largely improved knowledge of the parton distributions has been achieved, in particular at low x. QCD has been tested extensively and successfully, from the breakdown of perturbative QCD at low Q^2, up to the highest Q^2 where the small excess of events observed by H1 and ZEUS remains compatible with the Standard Model.

The future will bring new exciting results since about 50 pb^{-1} of e^-p data are expected in 1999-2000 which will complement the e^+p results presented here. New measurements of α_S, xg, and of the parton distribution functions will become available. The slight excess observed at high Q^2 will be also tested in e^-p.

Afterwards with the luminosity upgrade of HERA and its detectors in between 2000 and 2005, 500-1000 pb^{-1} of integrated luminosity are expected. Thus this program will continue with higher precision and with an extended potential for searching for deviations to the Standard Model.

Acknowledgments

I would like to thank the organizers of the SLAC topical workshop for their invitation to talk at this inspiring meeting, and all my colleagues of HERA and of the H1 and ZEUS collaborations for the results presented in this paper. Thanks also to Martin Erdmann and Stefan Schlenstedt for the careful reading of the manuscript. A very special thank to Ursula Bassler for her great help in the preparation of the talk and in the writing of the manuscript.

References

[1] H1 Collab., I. Abt *et al.*, Nucl. Phys. **B407** (1993) 515; H1 Collab., T. Ahmed *et al.*, Nucl. Phys. **B439** (1995) 471.

[2] ZEUS Collab., M. Derrick *et al.*, Phys. Lett. **B316** (1993) 412; ZEUS Collab., M. Derrick *et al.*, Z. Phys. **C65** (1995), 379.

[3] H1 Collab., S. Aid *et al.*, Nucl. Phys. **B470** (1996) 3.

[4] ZEUS Collab., M. Derrick *et al.*, Z. Phys. **C72** (1996) 399.

[5] H1 Collab., T. Ahmed *et al.*, Phys. Lett. **B324** (1994) 241; H1 Collab., S. Aid *et al.*, Z. Phys. **C67** (1995) 565; H1 Collab., S. Aid *et al.*, Phys. Lett. **B379** (1996) 319.

[6] ZEUS Collab., M. Derrick *et al.*, Phys. Rev. Lett. **75** (1995) 1006; ZEUS Collab., M. Derrick *et al.*, Z. Phys. **C72** (1996) 47.

[7] U. Bassler and G. Bernardi, Nucl. Instrum. Methods **A426** (1999) 583.

[8] A. Blondel and F. Jacquet, *Proceedings of the Study of an ep Facility for Europe*, ed. U. Amaldi, DESY 79/48 (1979) 391.

[9] U. Bassler and G. Bernardi, Nucl. Instr. Meth. **A361** (1995) 197.

[10] S. Bentvelsen *et al.*, *Proceedings of the Workshop Physics at HERA*, vol. 1, eds. W. Buchmüller and G. Ingelman, DESY (1992) 23.
C. Hoeger, ibid., 43.

[11] H1 Collab., C. Adloff *et al.*, Nucl. Phys. **B497** (1997) 3.

[12] ZEUS Collab., M. Derrick *et al.*, Z. Phys. **C69** (1996) 607; ZEUS Collab., J. Breitweg *et al.*, Phys. Lett. **B407** (1997) 432.

[13] L. N. Hand, Phys. Rev. **129** (1963) 1834; S. D. Drell and J. D. Walecka, Ann. Phys. **28** (1964) 18; F. J. Gilman, Phys. Rep. **4C** (1972) 95.

[14] B. L. Ioffe, Phys. Lett. **40** (1969) 123; B. L. Ioffe, V. A. Khoze, and L. N. Lipatov, *Hard Processes*, North Holland (1984) 185.

[15] A. Donnachie and P. V. Landshoff, Z. Phys. **C61** (1994) 139.

[16] M. Glück, E. Reya, and A. Vogt, Z. Phys. **C67** (1995) 433.

[17] Yu. L. Dokshitzer, Sov. Phys. JETP **46** (1977) 641; V. N. Gribov and L. N. Lipatov, Sov. J. Nucl. Phys. **15** (1972) 438 and 675;
G. Altarelli and G. Parisi, Nucl. Phys. **B126** (1977) 297.

[18] J. J. Sakurai, Ann. Phys. **11** (1960) 1.

[19] T. Bauer *et al.*, Rev. Mod. Phys. **50** (1978) 261.

[20] J. J. Sakurai and D. Schildknecht, Phys. Lett. **B40** (1972) 121.

[21] D. Schildknecht and H. Spiesberger, BI-TP-97-25 (1997) [hep-ph/9707447].

[22] H. Abramowicz *et al.*, Phys. Lett. **B269** (1991) 465; H. Abramowicz and A. Levy, DESY 97-251 (1997) [hep-ph/9712415].

[23] K. Adel, F. Barreiro, and F. J. Yndurain, Nucl. Phys. **B495**, 221 (1997).

[24] ZEUS Collab., Eur. Phys. J. **C7** (1999) 609.

[25] H1 Collab., "Precision Measurement of the Inclusive Deep Inelastic *ep* Scattering Cross-Section at Low Q^2 at HERA," ICHEP 98-Vancouver, 98-534.

[26] ZEUS Collab., "Measurement of the Proton Structure Function F2 in e+p Collisions at HERA," ICHEP 98-Vancouver, 98-769.

[27] E. A. Kuraev, L. N. Lipatov, and V. S. Fadin, Sov. Phys. JETP **45** (1977) 199; Y. Y. Balitsky and L. N. Lipatov, Sov. J. Nucl. Phys. **28** (1978) 822.

[28] H1. Collab., C. Adloff *et al.*, Phys. Lett. **393B** (1997) 452.

[29] H1 Collab., "A Measurement of the Inclusive Deep Inelastic *ep* Scattering Cross-Section at low Q^2 at HERA," IECHEP 97-Jerusalem, 97-260 (1997).

[30] B. W. Harris and J. Smith, Nucl. Phys. **B452** (1995) 109; B. W. Harris and J. Smith, Phys. Lett. **B353** (1995) 535.

[31] P. Bruni, G. Ingelman, and A. Solano, *Proceedings of the Workshop Physics at HERA*, vol. 1, eds. W. Buchmüller and G. Ingelman, DESY (1992) 363.

[32] G. Ingelman, L. Jönsson, and M. Nyberg, Phys. Rev. **D47** (1993) 4872.

[33] A. Ali *et al.*, *Proceedings of the Workshop Physics at HERA*, vol. 1, eds. W. Buchmüller and G. Ingelman, DESY (1992) 393; A. Ali *et al.*, *Proceedings of the Workshop Physics at HERA*, vol. 2, eds. W. Buchmüller and G. Ingelman, DESY (1992) 667.

[34] M. L. Mangano and P. Nanson, Phys. Lett. **B285** (1988) 160; M. H. Seymour, Z. Phys. **C63** (1994) 99; M. H. Seymour, Nucl. Phys. **B436** (1995) 16.

[35] S. J. Brodsky *et al.*, Phys. Lett. **B93** (1980) 451; S. J. Brodsky *et al.*, Nucl. Phys. **B369** (1992) 519.

[36] E. Laenen *et al.*, Nucl. Phys. **B392** (1993) 162, 229; E. Laenen *et al.*, Phys. Lett. **B291** (1992) 325; S. Riemersma, J. Smith, and W. L. van Neerven, Phys. Lett. **B347** (1995) 143.

[37] M. Glück, E. Reya, and M. Stratmann, Nucl. Phys. **B422** (1994) 37.

[38] H1 Collab., C. Adloff *et al.*, Z. Phys. **C72** (1996) 563; H1 Collab., "$D^{*\pm}$ Meson Production in DIS at HERA," ICHEP 98-Vancouver, 98-540.

[39] ZEUS Collab., J. Breitweg *et al.*, Phys. Lett. **B407** (1997) 402; ZEUS Collab., "Measurement of the D^* Cross-Section and the Charm Structure Function fo the Proton in Deep Inelastic Scattering at HERA," ICHEP 98-Vancouver, 98-768.

[40] ZEUS Collab., "Measurement of the Charm Structure Function of the Proton in Deep Inelastic Scattering using Semileptonic Charm Decays," ICHEP 98-Vancouver, 98-772.

[41] Particle Data Group, R. M. Barnett *et al.*, Phys. Rev. **D54** (1996) 1.

[42] B. W. Harris and J. Smith, hep-ph/9706334.

[43] C. Peterson *et al.*, Phys. Rev. **D27** (1983) 105.

[44] ARGUS Collab., H. Albrecht *et al.*, Phys. Lett. **B278** (1992) 202.

[45] NMC Collab., M. Arneodo *et al.*, Nucl. Phys. **B483** (1997) 3.

[46] H1 Collab., "A Measurement of the Inclusive Deep-Inelastic *ep* Scattering Cross-Section at Low Q^2 at HERA," IECHEP-97, 97-260 (1997).

[47] A. D. Martin, R. G. Roberts, and W. J. Stirling, Phys. Lett. **B387** (1996) 419.

[48] H. Lai *et al.*, Phys. Rev. **D55** (1997) 1280.

[49] H1 Collab., "Determination of the Gluon Density in the Proton from Charm Electro- and Photo-Production using NLO QCD," ICHEP 98-Vancouver, 98-538.

[50] S. Frixione *et al.*, Phys. Lett. **B348** (1995) 3.

[51] U. Katz, "New HERA Results on Deep-Inelastic e^+p Scattering at Very High Q^2," *these proceedings*.

[52] H1 Collab., C. Adloff *et al.*, Z. Phys. **C74** (1997) 191.

[53] ZEUS Collab., J. Breitweg *et al.*, Z. Phys. **C74** (1997) 207.

[54] H1 Collab., "A Search for Leptoquark Bosons in DIS at High Q^2 at HERA", ICHEP 98-Vancouver, 98-580.

[55] ZEUS Collab., "Resonance Search in *ep* Scattering at High x and Q^2 Using the ZEUS Detector at HERA," ICHEP 98-Vancouver, 98-754.

[56] H1 Collab., "Measurement of Inclusive Cross-Sections for Neutral and Charged Current Interactions at High-Q^2," ICHEP 98-Vancouver, 98-533.

[57] ZEUS Collab., "Measurement of High-Q^2 Neutral-Current DIS Cross-Sections at HERA," ICHEP 98-Vancouver, 98-752.

[58] ZEUS Collab., "Measurement of High-Q^2 Charged-Current DIS Cross-Sections at HERA," ICHEP 98-Vancouver, 98-751.

[59] A. Martin *et al.*, Eur. Phys. J. **C4** (1998) 463.

[60] BCDMS Collab., A. C. Benvenuti *et al.*, Phys. Lett. **B223** (1989) 485; Phys. Lett. **B237** (1990) 592.